

Supernova Precursor Emission and the Origin of Pre-Explosion Stellar Mass-Loss

TATSUYA MATSUMOTO¹ AND BRIAN D. METZGER^{1,2}

¹*Department of Physics and Columbia Astrophysics Laboratory, Columbia University, Pupin Hall, New York, NY 10027, USA*

²*Center for Computational Astrophysics, Flatiron Institute, 162 5th Ave, New York, NY 10010, USA*

ABSTRACT

A growing number of core collapse supernovae (SNe) which show evidence for interaction with dense circumstellar material (CSM) are accompanied by “precursor” optical emission rising weeks to months prior to the explosion. The precursor luminosities greatly exceed the Eddington limit of the progenitor star, implying they are accompanied by substantial mass-loss. Here, we present a semi-analytic model for SN precursor light curves which we apply to constrain the properties and mechanisms of the pre-explosion mass-loss. We explore two limiting mass-loss scenarios: (1) an “eruption” arising from shock break-out following impulsive energy deposition below the stellar surface; (2) a steady “wind” due to sustained heating of the progenitor envelope. The eruption model, which resembles a scaled-down version of Type IIP SNe, can explain the luminosities and timescales of well-sampled precursors, for ejecta masses $\sim 0.1 - 1 M_{\odot}$ and velocities $\sim 100 - 1000 \text{ km s}^{-1}$. By contrast, the steady-wind scenario cannot explain the highest precursor luminosities $\gtrsim 10^{41} \text{ erg s}^{-1}$, under the constraint that the total ejecta mass not exceed the entire progenitor mass (though the less-luminous SN 2020tlf precursor can be explained by a mass-loss rate $\sim 1 M_{\odot} \text{ yr}^{-1}$). However, shock interaction between the wind and pre-existing (earlier ejected) CSM may boost its radiative efficiency and mitigate this constraint. In both eruption and wind scenarios the precursor ejecta forms compact ($\lesssim 10^{15} \text{ cm}$) optically-thick CSM at the time of core collapse; though only directly observable via rapid post-explosion spectroscopy (\lesssim few days before being overtaken by the SN ejecta), this material can boost the SN luminosity via shock interaction.

Keywords: XXX

1. INTRODUCTION

A fraction of massive stars undergo strongly enhanced mass-loss near the very ends of their lives, forming a dense circumstellar medium (CSM) around themselves (e.g., Smith 2014). When the stars explode as supernovae (SNe), the CSM manifests through narrow emission lines in the optical spectra generated by the as-yet-unshocked slowly expanding CSM, photoionized by the SN light (e.g., SN Type IIn, Ibn or Icn, depending on whether the spectrum is hydrogen-rich, hydrogen-poor but helium-rich, or both hydrogen- and helium-poor, respectively; Schlegel 1990; Filippenko 1997; Foley et al. 2007; Pastorello et al. 2008; Nyholm et al. 2020; Gal-Yam et al. 2022; Fraser et al. 2021). The related technique of “flash spectroscopy” (e.g., Gal-Yam et al. 2014; Khazov et al. 2016) demonstrates that the progenitor’s mass-loss rate is elevated just before core collapse, among a significant fraction of even nominally CSM-free SNe (e.g., Yaron et al. 2017; Bruch et al. 2021).

The light curves of some of the most luminous SNe are powered at least in part by shock interaction between the SN ejecta and dense CSM released from the progenitor star in the days to weeks to years prior to its terminal core collapse (e.g., Smith & McCray 2007; Chevalier

& Irwin 2011; Ginzburg & Balberg 2012; Svirski et al. 2012; McDowell et al. 2018; Suzuki et al. 2019). At typically larger radii and lower densities, CSM shock interaction can also produce thermal and non-thermal X-ray and radio emission (e.g., Chandra et al. 2012; Margutti et al. 2014; Dwarkadas et al. 2016; Chakraborti et al. 2016; Margutti et al. 2017; Chiba et al. 2020).

If the pre-SN stellar mass-loss is modeled as a steady wind, the inferred mass-loss rates in Type IIn SNe, $\dot{M} \sim 10^{-4} - 0.1 M_{\odot} \text{ yr}^{-1}$ (Fox et al. 2011; Kiewe et al. 2012; Moriya et al. 2014), are significantly larger than can be explained by line-driven winds $\dot{M} \lesssim 10^{-5} M_{\odot} \text{ yr}^{-1}$ (Vink et al. 2001; Smith 2014). Instead, several alternative physical processes have been proposed to give rise to enhanced mass-loss just prior to core collapse. Mass-loss can occur due to intense heating of the stellar envelope by damping of waves excited by vigorous convection in the stellar core (e.g., Quataert & Shiode 2012; Shiode & Quataert 2014; Fuller 2017; Fuller & Ro 2018; Leung & Fuller 2020; Wu & Fuller 2022). In this scenario, the timing of the mass-loss should correspond to late stages of nuclear burning, which occurs on timescales of days to weeks prior to explosion for silicon burning; to several years for oxygen and neon burning (e.g., Woosley et al. 2002). Another mechanism for generating pre-SN

mass-loss invokes sudden energy release deep inside the star due to instabilities associated with late-stages of nuclear shell burning (e.g., Meakin & Arnett 2007; Smith & Arnett 2014; Fields & Couch 2021; Varma & Müller 2021; Yoshida et al. 2021). Mass-loss due to interaction with a close binary companion may also play a role in some events (e.g., Chevalier 2012; McIey & Soker 2014; Sun et al. 2020). In very massive rotating stars which experience efficient mixing, centrifugally-induced mass-loss may accompany contraction during the star’s final burning stages (e.g., Aguilera-Dena et al. 2018).

“Precursor” outbursts prior to the main SN explosion (e.g., Ofek et al. 2014) offer a clue to distinguishing these various mass-loss mechanisms. Several precursor events accompanying interacting SNe have been observed in recent years typically weeks to months prior to the main explosion, the most well-studied of which accompanied SN 2009ip (Fraser et al. 2013; Mauerhan et al. 2013; Pastorello et al. 2013; Prieto et al. 2013; Graham et al. 2014; Margutti et al. 2014; Mauerhan et al. 2014; Levesque et al. 2014; Martin et al. 2015; Graham et al. 2017; Reilly et al. 2017; Smith et al. 2022), 2010mc (Ofek et al. 2013), 2015bh (Elias-Rosa et al. 2016; Ofek et al. 2016; Thöne et al. 2017; Jencson et al. 2022), 2016bhu (Pastorello et al. 2018), LSQ13zm (Tartaglia et al. 2016), and 2020tlf (Jacobson-Galán et al. 2022) as well as the implication of pre-SN activity in SN 2010bt (Elias-Rosa et al. 2018), 2013gc (Reguitti et al. 2019), 2018cnf (Pastorello et al. 2019), 2019zrk (Fransson et al. 2022), 2021foa (Reguitti et al. 2022), and 19 events compiled in Strotjohann et al. (2021). Efforts to monitor a large number of massive stars in nearby galaxies to determine which explode as SNe (Kochanek et al. 2008) and systematic analyses of interacting SNe (Ofek et al. 2014; Bilinski et al. 2015; Strotjohann et al. 2021), rule out luminous precursors accompanying all SNe (Kochanek et al. 2017; Johnson et al. 2018). However, Strotjohann et al. (2021) found that $\simeq 25\%$ of Type II_n SNe (themselves accounting for $\simeq 10\%$ of core collapse SNe; e.g., Perley et al. 2020) exhibit precursors brighter than -13 mag (or luminosity $\gtrsim 5 \times 10^{40}$ erg s $^{-1}$) three months before the SN explosion.

Figure 1 and Table 1 summarize the bolometric light curves and other observable properties of a set of well-sampled SN precursors. Most of these SNe are classified as Type II, so we focus in this work on precursors from hydrogen-rich stars (though precursor outbursts have also been observed in some hydrogen-poor SNe; e.g.,

Foley et al. 2007; Pastorello et al. 2008).¹ The luminosities of the observed precursors $\sim 10^{40} - 10^{41}$ erg s $^{-1}$ are typically well above the Eddington limit for typical SN progenitor stars of mass $\simeq 10 - 20 M_{\odot}$,² indicating that this emission phase is accompanied by substantial mass-loss, which should then contribute to CSM interaction with the supernova light or ejecta in the post-explosion phase.

In this paper, we present a model for the light curves of SN precursors from hydrogen-rich stars, which we apply to the observed precursor sample in order to constrain the pre-SN mass-loss phase. With the exception of radiation hydrodynamical simulations by Dessart et al. (2010), few previous theoretical works have attempted to model the precursor emission phase. Instead, most constraints on the mass and radial distribution of the CSM around SN progenitors have come from the post-explosion interaction (e.g., Smith & McCray 2007; Chevalier & Irwin 2011; Chatzopoulos et al. 2013; McDowell et al. 2018; Suzuki et al. 2019). Though our light curve model makes several simplifying assumptions, these same features make it flexible and applicable to a wide parameter space of potential pre-explosion mass-loss behavior. As we shall discuss, we find that the bulk of the CSM generated during the observed precursor outbursts will usually be located so close to the progenitor star at the time of the explosion as to be quickly overtaken by the SN ejecta, making this material challenging to directly observe by other means.

This paper is organized as follows. In Section 2 we introduce two idealized models for the nature of the pre-SN mass-loss phase (dynamical “eruption” versus steady “wind”) and describe our model for calculating the precursor light curve from each case. In Section 3 we present the results of our light curve calculations and interpret them analytically. We also assess the ability of the eruption and wind models to explain the observed SN precursor events and determine the ejecta parameters required in each case. We discuss the resulting CSM from precursor events in Section 4 and finally summarize our results and conclude in Section 5.

2. PRECURSOR EMISSION MODEL

¹ Some massive stars also generate bright eruptions—so-called “giant eruptions” in luminous blue variable phase or “SN imposters” (e.g., Pastorello et al. 2010; Pastorello & Fraser 2019), which are potentially related to instabilities in massive star envelopes (e.g., Humphreys & Davidson 1994; Owocki 2015; Jiang et al. 2018) and accompanied by mass-loss (e.g., Gal-Yam et al. 2007; Gal-Yam & Leonard 2009), but typically are not coincident with the terminal core collapse event. Here we focus on SN precursors which precede the terminal explosion by at most a few years and thus are likely to be causally connected to late-stages of nuclear burning.

² The progenitors of SN 2009ip and 2015bh may be more massive $\gtrsim 35 - 50 M_{\odot}$ (Smith et al. 2010; Foley et al. 2011; Boian & Groh 2018).

Table 1. Observed Properties of SN Precursor Emission

Event	$L_{\text{pre}}^{(a)}$ [erg/s]	$t_{\text{pre}}^{(b)}$ [d]	$E_{\text{pre}}^{(c)}$ [erg]	v_{obs} [10^3 km/s]	Ref.
SN 2009ip	3.6×10^{41}	44 [¶]	1.4×10^{48} [¶]	0.8-1.4, 8-9, 14-15 [‡]	1,2,3
SN 2010mc	1.6×10^{41}	31	4.4×10^{47}	1-3 (6 d) [†]	4
SN 2015bh	9.3×10^{40}	95 [¶]	7.6×10^{47} [¶]	0.6-1, 0.9-1.5, 2.6-6 [‡]	5
SN 2016bdu	1.2×10^{41}	97 [¶]	1.0×10^{48} [¶]	0.4 ($\simeq 10$ d) [†]	6
SN 2020tlf	8.8×10^{39}	127	9.7×10^{46}	0.05-0.2 (10 d) [†]	7

(*a*) Average luminosity of precursor emission, defined as $L_{\text{pre}} = E_{\text{pre}}/t_{\text{pre}}$.

(*b*) Duration from the first precursor detection to the time of the SN explosion.

(*c*) Total radiated energy of the precursor emission.

[¶]Lower limit due to the lack of detection or flux upper limit.

[‡]Obtained via spectroscopy during the precursor emission itself. The H α line profile is fitted by multiple velocity components.

[†]Obtained via flash-spectroscopy t_{flash} (shown in parentheses) after the SN explosion. Note that these velocities are sometimes too low to be associated with mass ejection responsible for the precursor emission because the latter would have been overtaken by the SN ejecta by the time of the flash-spectroscopy (t_{flash}).

Ref. 1: Mauerhan et al. (2013), **2:** Pastorello et al. (2013),

3: Margutti et al. (2014), **4:** Ofek et al. (2013), **5:** Elias-Rosa et al. (2016),

6: Pastorello et al. (2018), **7:** Jacobson-Galán et al. (2022).

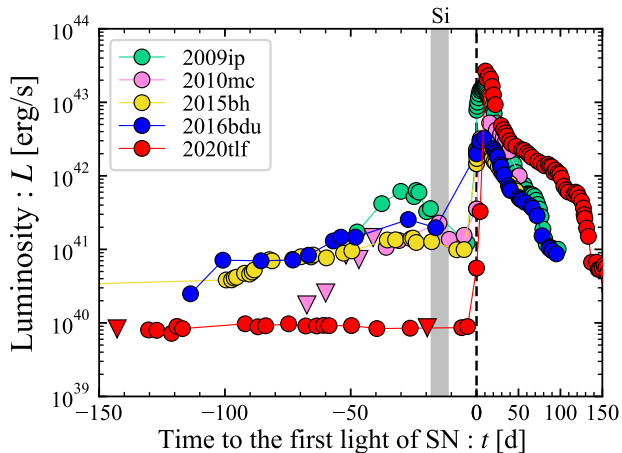


Figure 1. Sample of SN precursor light curves, showing the luminosity as a function of time relative to the onset of the SN (which we define by the luminosity rising abruptly by a factor of $\gtrsim 10$). Shaded region shows the characteristic timescale range before core collapse corresponding to core silicon burning in $13 - 20 M_{\odot}$ stars (Woosley et al. 2002). References to the light curve data are given in Table 1.

We calculate SN precursor light curves largely following the semi-analytical model developed in Matsumoto & Metzger (2022); Metzger et al. (2021). The general approach is as follows: the pre-SN mass-loss is divided

into multiple ejecta shells ordered based on their velocity, and for each shell we calculate its thermal evolution and resulting emission by means of a one-zone model. The total light curve is then obtained by summing the luminosity contributions from each shell. For simplicity we assume the ejecta to be spherically symmetric, even though in some mass-loss scenarios it could possess a non-spherical (e.g., equatorial disk-like) geometry.

A key input to the model is the velocity distribution of the pre-SN ejecta. We explore two physically-motivated scenarios for its form, which bracket extremes along a continuum of possible behaviors.

1. An “eruption,” in which mass-loss occurs in a single event on a timescale comparable or less than the dynamical time at the ejection radius. Physically, a temporally-concentrated injection of energy deep inside the star generates a shock wave, which propagates radially outwards and accelerates the stellar envelope, unbinding a portion of its mass (Dessart et al. 2010; Kuriyama & Shigeyama 2020; Linial et al. 2021; Ko et al. 2021). Although we remain indifferent to the origin of the sudden energy injection, one possible physical realization would be a dynamical instability associated with unstable nuclear shell burning.
2. A continuous “wind,” in which mass-loss occurs from the star at a roughly constant rate, over timescales much longer than the dynamical time.

Physically, this is expected to occur when the stellar envelope is heated well above the Eddington luminosity at a roughly constant rate (e.g., [Smith & Owocki 2006](#); [Quataert et al. 2016](#)). This scenario may be approximately realized in wave-heating scenarios (e.g., [Quataert & Shiode 2012](#); [Fuller 2017](#)).

The following subsections describe the eruption and wind scenarios individually. Throughout this work we assume that the precursor emission arises directly from a single mass-loss event or mass-loss phase prior to the terminal explosion; however, we caution that some events may arise from more complicated circumstances (e.g., multiple episodes of mass-loss giving rise to collisions between ejecta shells; dim SNe followed by bright CSM interaction; or binary star mergers) in particular for SN 2009ip (e.g., [Pastorello et al. 2013](#); [Soker & Kashi 2013](#); [Smith et al. 2014](#)).

2.1. Eruption Scenario

In the eruption scenario, energy is injected suddenly into the stellar envelope, driving a shock wave towards its surface (e.g., [Dessart et al. 2010](#)). As a result, we assume the ejecta achieve a homologous density profile $\rho(v = r/t)$, defined such that $M_{\text{ej}}(> v) = 4\pi \int_v^\infty \rho(v)r^2 dr$ is the ejecta mass above a given velocity v .

Depending on the magnitude of the injected energy, the ejecta can be accelerated to an arbitrarily high velocity as long as the latter exceeds the escape speed at the radius R_0 matter is ejected (e.g., [Linial et al. 2021](#)),

$$v_{\text{esc}} = \sqrt{\frac{2GM_\star}{R_0}} \quad (1)$$

$$\simeq 200 \text{ km s}^{-1} \left(\frac{M_\star}{10 M_\odot} \right)^{1/2} \left(\frac{R_0}{10^2 R_\odot} \right)^{-1/2}, \quad (2)$$

where G is the gravitational constant and M_\star is the progenitor mass. Spectroscopic observations of SN precursors, in the few cases available, indicate high ejecta speeds $\sim 10^2 - 10^3 \text{ km s}^{-1}$ (Table 1). This suggests the deposited energy being comparable to the stellar binding energy if released at radii $R_0 \sim 1 - 100 R_\odot$ deep below the surface $R_\star \sim 10^3 R_\odot$ of a RSG progenitor (or with energy greatly exceeding the local binding energy if deposited closer to the surface).

We now describe our method to calculate the emission from a single shell of mass M and velocity v ejected at $t = 0$ from radius R_0 . The radial distance of the shell from the progenitor's center is given by $R = v \cdot t + R_0$ and its volume is given by $V = 4\pi R^2 \Delta R$, where ΔR is the width of the shell. For a homologously expanding ejecta, the width is given by $\Delta R = dv \cdot t + \Delta R_0$, where dv is the velocity difference from the next shell and ΔR_0 is the initial width of the shell. The initial internal energy of the shell is assumed to equal its kinetic energy $E_0 =$

$Mv^2/2$.³ The internal energy is comprised of ideal gas, radiation, and ionization energy:

$$E = \frac{3}{2}(1 + \bar{x})Nk_{\text{B}}T + aT^4V + \sum_i NA_i x_i \varepsilon_i, \quad (3)$$

where $\bar{x} = \sum_i A_i x_i$, A_i , x_i , and ε_i are the mean ionization degree, abundance fraction, degree of ionization, and ionization energy of species i , respectively. We calculate \bar{x} and x_i by solving the Saha equation taking into account singly-ionized hydrogen and helium. The other quantities are the total number of nuclei N , the Boltzmann constant k_{B} , temperature T , and radiation constant a .

The thermal evolution of the ejecta is described by the first law of thermodynamics:

$$\frac{dE}{dt} = -(\gamma_3 - 1)\frac{E}{V}\frac{dV}{dt} - L, \quad (4)$$

where γ_3 and L are the adiabatic index and radiated luminosity, respectively. In the adiabatic loss term, we have used the fact the pressure is given by $P = (\gamma_3 - 1)E/V$. The adiabatic index is calculated from the density, temperature, and the ionization state of the shell as in [Matsumoto & Metzger \(2022\)](#); [Kasen & Ramirez-Ruiz \(2010\)](#). The radiative loss term is approximated by the photon diffusion luminosity

$$L = \frac{E_{\text{rad}}}{S(t)t_{\text{d}} + t_{\text{lc}}}, \quad (5)$$

where $E_{\text{rad}} = aT^4V$ is the radiation's internal energy, t_{d} is the photon diffusion time, and $S(t)$ is a suppression factor discussed below. The diffusion time is that over which photons escape radially through the ejecta,

$$t_{\text{d}} = \frac{R\tau}{c} \quad \text{and} \quad \tau = \int_R \kappa \rho dr, \quad (6)$$

where c is the speed of light and $\kappa(\rho, T)$ is Rossland-mean opacity, which we approximate using the analytic expression provided in [Matsumoto & Metzger \(2022\)](#) for solar metallicity composition material. The dominant form of opacity near peak light is electron scattering (under conditions of partial or full ionization), though Kramer's opacity can become relevant at high densities and low temperatures. The suppression factor,

$$S(t) \equiv \frac{e^{t_{\text{d}}/t} - 1}{t_{\text{d}}/t}, \quad (7)$$

³ In detail, for this initial condition, the shell will accelerate after the ejection by PdV work within several dynamical times $\sim R_0/v$; however, since the increase of the velocity is by at most a factor of $\sqrt{2} \simeq 1.4$, we neglect this acceleration phase and assume the shells expand at constant velocity from $t = 0$.

acts to reduce the radiative losses exponentially for $t \ll t_d$. Without this correction, the luminosities of all radiation-pressure-dominated shells reach a value $L \propto R_0 v / \kappa$ starting immediately after their ejection and contribute almost equally (up to a factor of v) regardless of their optical depth; this behavior is unphysical, however, because at $t \lesssim t_d$ most photons are still trapped within ejecta and only the tiny fraction in the “diffusion tail” can escape (see also Piro & Nakar 2013). The light crossing time $t_{lc} = R/c$ in the denominator of Eq. (5) limits the photon escape timescale from the system at late times.

The mass profile of the ejecta depends on the details of the ejection process. The process of shock-breakout motivates a power-law profile (Nakar & Sari 2010),

$$M_{\text{ej}}(> v) = M_{\text{ej}}(v/v_{\text{ej}})^{-\beta}, \quad v > v_{\text{ej}}, \quad (8)$$

where M_{ej} is the total ejecta mass and v_{ej} is the minimum velocity. Assuming the stellar envelope can be described as a polytrope of index n , and that the energy injection occurs close to the stellar surface, then we can set the initial radius $R_0 \sim R_*$ for all shells and the process of shock breakout will impart a self-similar velocity profile of the form $v \propto \rho^{-\mu}$ (Gandel’Man & Frank-Kamenetskii 1956; Sakurai 1960), where $\mu \simeq 0.22$ (for $n = 3/2$) and $\mu = 0.19$ (for $n = 3$). Since the density profile and external mass in this scenario obey $\rho \propto x^n$ and $M(> r) \propto \rho x R_*^2$, where $x = R_* - r$ is the depth measured from the surface, the power-law index entering Eq. (8) in this scenario becomes $\beta = (n + 1)/\mu n \simeq 7.6$ for $n = 3/2$ and 7.0 for $n = 3$. The shock breakout solution also gives a relation between the velocity and initial depth of each shell $v = v_{\text{ej}}(x/x_{\text{ej}})^{-\mu n}$, where the depth of the innermost slowest shell ($v = v_{\text{ej}}$) obeys $x_{\text{ej}}/R_* \sim (M_{\text{ej}}/M_*)^{\frac{1}{n+1}}$. The initial width of each shell is likewise given by

$$\Delta R_0(v) = \left| \frac{dx}{dv} \right| dv = \frac{x_{\text{ej}}}{\mu n v_{\text{ej}}} \left(\frac{v}{v_{\text{ej}}} \right)^{-\frac{\mu n + 1}{\mu n}} dv. \quad (9)$$

Note that above prescription holds only for energy injected into layers of the star close to the surface ($R_0 \sim R_*$ and $M_{\text{ej}} \ll M_*$). Nevertheless, in what follows we shall apply $R_0 = R_*$ also to the eruptions with greater ejecta masses, seeded by energy deposition at deeper layer $\ll R_*$. Realistically, after the shock passage, each mass shell is quickly imparted comparable internal and kinetic energies, and hence the initial radius R_0 should be smaller than R_* and different for each shell. While this complicated hydrodynamics should be studied by numerical approaches with more specific stellar models to set more accurate initial conditions, we assume for simplicity that all shells are ejected at $t = 0$ from R_* with equal internal and kinetic energies as adopted for analytical light curve modeling of SNe (Arnett 1980, 1982; Popov 1993). Physically, heating near the surface

will occur as the ejecta from deeper layers collides and shocks with material closer to the surface.

In summary, the eruption scenario is described by four main parameters: total ejecta mass M_{ej} , initial radius R_0 (which we canonically set to $R_0 = R_*$, motivated by the shock-breakout prescription), minimum ejecta speed v_{ej} (which must exceed v_{esc} ; Eq. 2), and the time of the eruption prior to the SN explosion, t_{erupt} . The power-law index of mass profile β is also a free parameter, though we shall take $\beta = 7.6$ as fiducial (corresponding to RSG progenitors), motivated by above discussion. Although the self-similar shock breakout solution described above holds only near the stellar surface, we find that the light curve properties are not sensitive to the precise value of β for otherwise fixed values of M_{ej} and v_{ej} (see Matsumoto & Metzger 2022; their Fig. 6). We assume initial shell widths given by Eq. (9); however, the calculated light curve properties are also not sensitive to this choice (assuming a constant width for all shells, $\Delta R_0 = \text{const}$, gives a similar result). Relative to Matsumoto & Metzger (2022), the updates of our current model include: (1) the diffusion time calculated as a full radial integral (Eq. 6) instead of using a local estimate; (2) inclusion of the early-time suppression factor (Eq. 7).

For the assumed mass profile, the diffusion time is

$$t_d \simeq \frac{\beta}{\beta + 2} \frac{\kappa M(> v)}{4\pi c R} \underset{\beta=7.6}{\simeq} 240 \text{ d} \left(\frac{M(> v)}{M_\odot} \right) \left(\frac{R}{10^3 R_\odot} \right)^{-1}, \quad (10)$$

where the second equality assumes a constant electron scattering opacity $\kappa = \kappa_{\text{es}} \simeq 0.32 \text{ cm}^2 \text{ g}^{-1}$ (hereafter adopted to other analytic estimates unless otherwise specified). The total ejecta kinetic energy is given by

$$E_{\text{kin}} = \int_{v_{\text{ej}}} \frac{dM}{dv} \frac{v^2}{2} dv \simeq \frac{\beta}{2(\beta - 2)} M_{\text{ej}} v_{\text{ej}}^2 \underset{\beta=7.6}{\simeq} 5.2 \times 10^{47} \text{ erg} \left(\frac{M_{\text{ej}}}{M_\odot} \right) \left(\frac{v_{\text{ej}}}{v_{\text{esc}}} \right)^2 \left(\frac{M_*}{10 M_\odot} \right) \left(\frac{R_0}{10^2 R_\odot} \right)^{-1}. \quad (11)$$

Based on the physical requirement that the total energy radiated by SN precursors $E_{\text{pre}} \sim 10^{47} - 10^{48} \text{ erg}$ (Table 1) not exceed E_{kin} , we note that the minimum velocity must obey $v_{\text{ej}} \gtrsim 340 \text{ km s}^{-1} (E_{\text{pre}}/10^{48} \text{ erg})^{1/2} (M_{\text{ej}}/M_\odot)^{-1/2}$.

2.2. Wind Scenario

In the steady wind scenario, the precursor emission is generated by a mass outflow from the star with an assumed constant mass-loss rate \dot{M} and velocity v_w . We begin our calculation at the sonic radius R_s , where the thermal energy flux of the wind is comparable to its

kinetic power,

$$\dot{E}_w = \frac{1}{2} \dot{M} v_w^2 \simeq 1.2 \times 10^{40} \text{ erg s}^{-1} \times \left(\frac{\dot{M}}{M_\odot \text{ yr}^{-1}} \right) \left(\frac{v_w}{v_{\text{esc}}} \right)^2 \left(\frac{M_\star}{10 M_\odot} \right) \left(\frac{R_s}{10^2 R_\odot} \right)^{-1}, \quad (12)$$

where we have scaled the wind velocity to the escape speed v_{esc} at the sonic radius (Eq. 2, but replacing R_0 with R_s).

To treat the problem within the same framework as the eruption case, the wind is divided into shells of equal mass $M = \dot{M} \Delta t$, radius $R = v_w(t - t_0)$, width $\Delta R = v_w \Delta t$, and volume $V = 4\pi R^2 \Delta R$, where t_0 is the time a given shell is released relative to the start of the wind ($t = 0$) and Δt is the fixed time interval separating the ejection of successive shells. The procedure to calculate the light curve from each shell follows that of the eruption scenario, except that the suppression factor (Eq. 7) is now given by

$$S(t) = \frac{[e^{t_d/(t-t_0)} - 1]}{t_d/(t-t_0)}. \quad (13)$$

While the diffusion timescale is calculated by Eq. (6), its estimate is given by

$$t_d \simeq \frac{\kappa \dot{M}}{4\pi c v_w} \simeq 32 \text{ d} \left(\frac{\dot{M}}{M_\odot \text{ yr}^{-1}} \right) \times \left(\frac{v_w}{v_{\text{esc}}} \right)^{-1} \left(\frac{M_\star}{10 M_\odot} \right)^{-1/2} \left(\frac{R_s}{10^2 R_\odot} \right)^{1/2}, \quad (14)$$

which follows by taking the density as $\rho = \dot{M}/4\pi r^2 v_w$ (for a wind density profile $\rho \propto r^{-2}$, the diffusion time receives roughly equal contributions from all decades in radius; e.g., [Chevalier & Irwin 2011](#)).

In summary, the wind scenario is described by three parameters: wind mass-loss rate \dot{M} , wind velocity v_w (equivalently, sonic point R_s for a given progenitor mass M_\star), and the duration of the wind prior to the SN explosion t_w . Rather than define the latter as the entire duration of mass-loss prior to the explosion, t_{active} , we define t_w as the more limited duration over which the luminosity has reached its roughly constant value, i.e. $t_w = t_{\text{active}} - t_{\text{rise}}$, where t_{rise} is the light curve rise-time (see below, Sec. 3.2).

What range of wind properties are expected physically? [Quataert et al. \(2016\)](#) show that energy injection at some radius R_{in} below the stellar surface at a super-Eddington rate $\dot{E} \gg L_{\text{Edd}}$ drives a continuum radiation pressure-driven outflow. For sufficiently high values of $\dot{E} \gg \dot{E}_Q$, most of the injected power is eventually converted into the kinetic energy of the wind, i.e. $\dot{E}_w \simeq \dot{E}$,

where the threshold power is given by

$$\dot{E}_Q \equiv f^{5/2} \frac{M_{\text{env}} v_{\text{esc}}^5}{M_\star G} \simeq 2 \times 10^{40} \text{ erg s}^{-1} \times \left(\frac{f}{0.3} \right)^{5/2} \left(\frac{M_{\text{env}}}{10^{-2} M_\star} \right) \left(\frac{M_\star}{10 M_\odot} \right)^{5/2} \left(\frac{R_{\text{in}}}{10^2 R_\odot} \right)^{-5/2}. \quad (15)$$

Here, $M_{\text{env}} \lesssim 10^{-3} - 10^{-2} M_\star$ is the mass of the stellar envelope above the energy injection point up to the sonic radius and $f \sim 0.1 - 1$ is a dimensionless parameter that depends on the envelope structure ([Quataert et al. 2016](#); their Fig. 11). Thus, we typically have $\dot{E}_Q \sim 10^{39} - 10^{41} \text{ erg s}^{-1} \sim 1 - 100 L_{\text{Edd}}$, where the Eddington luminosity

$$L_{\text{Edd}} = \frac{4\pi G M_\star c}{\kappa_{\text{es}}} \simeq 1.6 \times 10^{39} \text{ erg s}^{-1} \left(\frac{M_\star}{10 M_\odot} \right). \quad (16)$$

In the limit $\dot{E} \gg \dot{E}_Q$, [Quataert et al. \(2016\)](#) show that the terminal velocity and mass-loss rate of the wind are related according to (their Eqs. 20, 26):

$$v_w \simeq 1.7 \left(\frac{M_\star}{M_{\text{env}}} G \dot{E} \right)^{1/5} \simeq 430 \text{ km s}^{-1} \times \left(\frac{M_{\text{env}}}{10^{-3} M_\star} \right)^{-1/5} \left(\frac{M_\star}{10 M_\odot} \right)^{1/5} \left(\frac{\dot{E}}{100 L_{\text{Edd}}} \right)^{1/5}, \quad (17)$$

$$\dot{M} \simeq 0.15 \frac{v_w^3}{G} \frac{M_{\text{env}}}{M_\star} \simeq 0.96 M_\odot \text{ yr}^{-1} \left(\frac{M_{\text{env}}}{10^{-3} M_\star} \right) \left(\frac{v_w}{300 \text{ km s}^{-1}} \right)^3. \quad (18)$$

The lower range of ejecta velocities inferred from SN precursor observations, $v_w \sim 100 - 500 \text{ km s}^{-1}$ (Table 1), can be obtained for $\dot{E} \sim 1 - 100 L_{\text{Edd}} \gtrsim \dot{E}_Q$ and $M_{\text{env}} \sim 10^{-4} - 10^{-2} M_\star$, corresponding to range of $\dot{M} \sim 1 - 100 M_\odot \text{ yr}^{-1}$. On the other hand, the higher end of the observed precursor velocity $\gtrsim 10^3 \text{ km s}^{-1}$ would require both a small envelope mass $M_{\text{env}} \lesssim 10^{-5} M_\star$ and large injection luminosity $\dot{E} \gtrsim 10^3 L_{\text{Edd}}$.

Although v_w represents the final velocity of the wind, [Quataert et al. \(2016\)](#) found that the initial expansion rate of the overlying envelope material, after the onset of heating, is significantly slower than v_w . This rising velocity inevitably leads to shock interaction between the wind and the overlying envelope material. Additional heating from such shocks may boost the transient luminosity compared to the constant-velocity wind modeled here (see Sec. 3.2.1).

3. RESULTS

We now summarize the light curve results, separately in the eruption and wind scenarios.

3.1. Eruption Scenario

Figure 2 shows example light curves in the eruption scenario, calculated for: $M_{\text{ej}} = 1 M_{\odot}$, $M_{\star} = 10 M_{\odot}$, $R_0 = R_{\star} = 10^3 R_{\odot}$, and $v_{\text{ej}} = 1000 \text{ km s}^{-1}$. The chosen values of stellar mass and radius are representative of RSG progenitors, while the velocity is motivated by those observed spectroscopically. The ejecta mass is chosen as needed to explain observed precursor luminosities (see Fig. 3). For these parameters, the ejecta is radiation-pressure-dominated and the light curve is powered by the escape of the initial internal energy. Hydrogen begins to recombine once the temperature decreases to a value $T_{\text{ion}} \sim 10^4 \text{ K}$, and the resulting sharp drop in opacity creates a well-defined recombination front. As the front recedes through the ejecta shell, this shapes a characteristic plateau in the light curve in the same way as in Type IIP SNe (Arnett 1980; Popov 1993; Kasen & Woosley 2009). The top panel shows the effective temperature, $T_{\text{eff}} = \left[L / (4\pi\sigma_{\text{SB}}R_{\text{ph}}^2) \right]^{1/4}$, where σ_{SB} is the Stefan-Boltzmann constant and the photosphere radius R_{ph} is defined by $\tau = \int_{R_{\text{ph}}} \kappa \rho dr = 2/3$.

Just after the eruption, the effective temperature is high and the peak of the assumed blackbody spectrum is in the UV range. We approximate the optical-wavelength light curve (black curve) by subtracting the UV luminosity (defined as radiation with frequency $\nu > 10^{15} \text{ Hz}$) from the bolometric luminosity (gray curve). Colored solid lines denote the single-shell light curves for different velocities ($v = 1000 \text{ km s}^{-1}$ to 1750 km s^{-1} , corresponding to colors from purple to red). As a result of the suppression factor (Eq. 7), low velocity shells do not contribute significantly to the total luminosity at early times, until their diffusion times become shorter than the expansion times.

In order to quantify the impact of new features of the light curve model introduced in this paper, a dashed line show the calculation performed with the original model of Matsumoto & Metzger (2022), which does not include the early-time suppression effect (Eq. 7) and used a local estimate for the radial optical depth rather than a full integral taken over the external shells. The new calculation light curve exhibits a shallower decay, but its overall luminosity and duration, do not change appreciably from the Matsumoto & Metzger (2022) model.

Due to the close similarity of the physical conditions in the precursor ejecta to that of Type IIP SNe, the characteristic luminosity and duration of the light curve can be estimated using the analytic expressions from

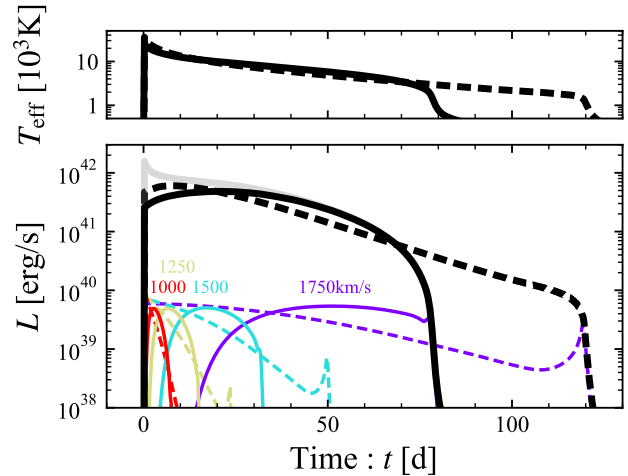


Figure 2. Example SN precursor light curve calculation in the eruptive mass-loss scenario. A solid black curve shows the optical light curve (bottom) and evolution of effective temperature (top) for a fiducial case with ejecta mass $M_{\text{ej}} = M_{\odot}$, initial radius $R_0 = R_{\star} = 10^3 R_{\odot}$, and minimum ejecta velocity $v_{\text{ej}} = 1000 \text{ km s}^{-1}$ for an assumed stellar mass $M_{\star} = 10 M_{\odot}$. The optical luminosity is calculated by excluding radiation of frequency $> 10^{15} \text{ Hz}$ from the bolometric light curve (gray curve). Colored solid lines show the luminosity contributed by single shells with velocity $v = 1000 \text{ km s}^{-1}$ to 1750 km s^{-1} (separated by 250 km s^{-1}) and shell width of $dv = 2 \text{ km s}^{-1}$. Dashed curves show an otherwise identical calculation calculated following the original model of Matsumoto & Metzger (2022), which neglects the early-time suppression factor (Eq. 7) and uses a local estimate for the radial optical depth.

Popov (1993):

$$L_{\text{Popov}} = 2.0 \times 10^{41} \text{ erg s}^{-1} \left(\frac{M_{\text{ej}}}{M_{\odot}} \right)^{1/3} \times \left(\frac{R_0}{10^3 R_{\odot}} \right)^{2/3} \left(\frac{v_{\text{ej}}}{10^3 \text{ km s}^{-1}} \right)^{5/3}, \quad (19)$$

$$t_{\text{Popov}} = 74 \text{ d} \left(\frac{M_{\text{ej}}}{M_{\odot}} \right)^{1/3} \left(\frac{R_0}{10^3 R_{\odot}} \right)^{1/6} \left(\frac{v_{\text{ej}}}{10^3 \text{ km s}^{-1}} \right)^{-1/3}, \quad (20)$$

where we have approximated the mean ejecta velocity as v_{ej} and have adopted a normalization calibrated from the radiative transfer simulations of Sukhbold et al. (2016) (see also Blagorodnova et al. 2021).

Figure 3 shows light curves in the eruption scenario, calculated for different variations of the ejecta parameters relative to the fiducial case in Fig. 2. The resulting changes in the plateau emission properties roughly agree with the analytic scaling relations in Eqs. (19), (20). For example, increasing the ejecta mass increases the dura-

tion and luminosity of the plateau, while increasing the minimum velocity increases the plateau luminosity but shortens its duration.

For comparison in Fig. 3 we show the light curves of observed SN precursors (Fig. 1). In order to roughly match the observations, we set the time of the eruption prior to core collapse to $t_{\text{erupt}} = 140, 100,$ and 50 days for $v_{\text{ej}} = 200 \text{ km s}^{-1}$ (black and yellow), 500 km s^{-1} (blue), and 1000 km s^{-1} (red), respectively. Before exploring the detailed model parameters required to fit the observations, we first note that—broadly speaking—the luminosities predicted in the outburst model, $L_{\text{pre}} \sim 10^{41} \text{ erg s}^{-1}$, match those of observed precursors. In detail, our outburst model predicts light curves which decay monotonically following the initial peak, in conflict with observed precursor emission (in particular, SN 2015bh and 2016bdu), which instead rises for a few months leading up to the SN. However, this discrepancy may at least in part arise from some of the simplifying assumptions of our model, such as the velocity profile and initial shell radii; indeed, the radiation hydrodynamic simulations of precursor outbursts by Dessart et al. (2010) predict rising light curves.⁴

Figure 4 shows an estimate of the plateau luminosity L_{pl} and duration t_{pl} , calculated from a large grid of models in the space of ejecta mass M_{ej} and ejecta velocity v_{ej} for different assumptions about initial (and progenitor) radii $R_0 = R_{\star} = 10, 10^2,$ and $10^3 R_{\odot}$. Here, we define the duration t_{pl} as that over which 90% of the total energy is radiated, $0.9E_{\text{pl}} = \int^{t_{\text{pl}}} L dt$, where $E_{\text{pl}} = \int L dt$. The average luminosity is then defined as $L_{\text{pl}} = E_{\text{pl}}/t_{\text{pl}}$. Note that the model-predicted plateau duration t_{pl} only represents an upper limit on the observed precursor duration if the SN explosion occurs before the end of the eruption emission phase. However, due to the relatively flat shape of the predicted light curve, the model-predicted value of L_{pl} will still be comparable to the time-averaged observed luminosity L_{pl} , even when the eruption emission is prematurely terminated by the SN.

The distributions of plateau luminosity and duration roughly follow those predicted by Eqs. (19) and (20), namely $M_{\text{ej}} \propto v_{\text{ej}}^{-5}$ and $M_{\text{ej}} \propto v_{\text{ej}}$, for fixed values of L_{Popov} and t_{Popov} , respectively. For lower ejecta velocities, comparable to the RSG surface escape speed $\sim 10 - 100 \text{ km s}^{-1}$, gas pressure instead of radiation pressure dominates in the ejecta and other assumptions of the Popov analytic estimates (e.g., the neglect of hydrogen recombination energy) are violated (Matsumoto & Metzger 2022). On the other hand, for ejecta masses $\sim M_{\odot}$, velocities $\sim 10^3 \text{ km s}^{-1}$, and radii close to the surface of the RSG progenitors ($R_0 \sim R_{\star} \sim 10^3 R_{\odot}$),

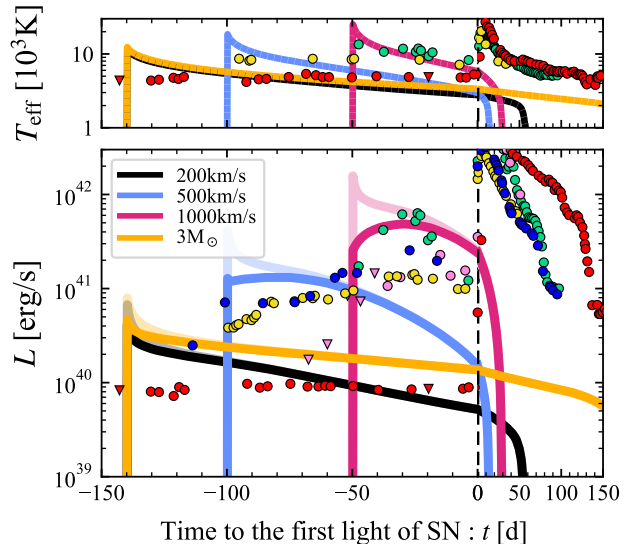


Figure 3. Same as in Fig. 2 but showing light curves in the eruption scenario for different ejecta parameters, and compared with observed SN precursors (Fig. 1). Blue, black, and red curves show models with a common ejecta mass $M_{\text{ej}} = M_{\odot}$ but different ejecta velocities $v_{\text{ej}} = 200, 500,$ and 1000 km s^{-1} , respectively. A yellow curve shows a model with $v_{\text{ej}} = 200 \text{ km s}^{-1}$ but larger $M_{\text{ej}} = 3 M_{\odot}$. Lighter shaded curves denote the bolometric luminosity. The stellar mass $M_{\star} = 10 M_{\odot}$ and radius $R_0 = 10^3 R_{\odot}$ are fixed for all models. The time of the eruption prior to the SN is set to $t_{\text{erupt}} = 140$ days (except for high-velocity models shown with blue and red curve, for which $t_{\text{erupt}} = 100$ and 50 d) to roughly match the onset of the observed precursor emission. The dependence of the predicted plateau luminosity and duration on the ejecta properties broadly agree with the Popov analytic scalings (Eqs. 19, 20).

the predicted transient properties are consistent with the observed precursors. The high required ejecta velocity exceeding the surface escape speed by factors $\gtrsim 10$ may point to energy deposition deep within the star $\sim 10 R_{\odot}$. To reproduce the observed precursors with $\sim 10^{41} \text{ erg s}^{-1}$ and $\sim 10^3 \text{ km s}^{-1}$ from more compact progenitor stars such as blue supergiants ($R_{\star} \sim 10 R_{\odot}$, see the bottom panel in Fig. 4), would require more massive ejecta $\gtrsim 3 M_{\odot}$.

3.2. Wind Scenario

Figure 5 shows examples of the light curve and effective temperature evolution in the wind mass-loss scenario, for a fixed progenitor mass $M_{\star} = 10 M_{\odot}$. A thick black curve depicts the chosen fiducial model, with wind mass-loss rate $\dot{M} = M_{\odot} \text{ yr}^{-1}$ and speed $v_w = 200 \text{ km s}^{-1}$ (corresponding to $R_s = 100 R_{\odot}$, Eq. 2). This mass loss rate is broadly motivated by observed Type IIn SNe, though is somewhat higher than the values typically in-

⁴ Adopting the same ejecta parameters as Dessart et al. (2010), our calculation predicts a plateau luminosity and duration that agree with their numerical results to within a factor of a few.

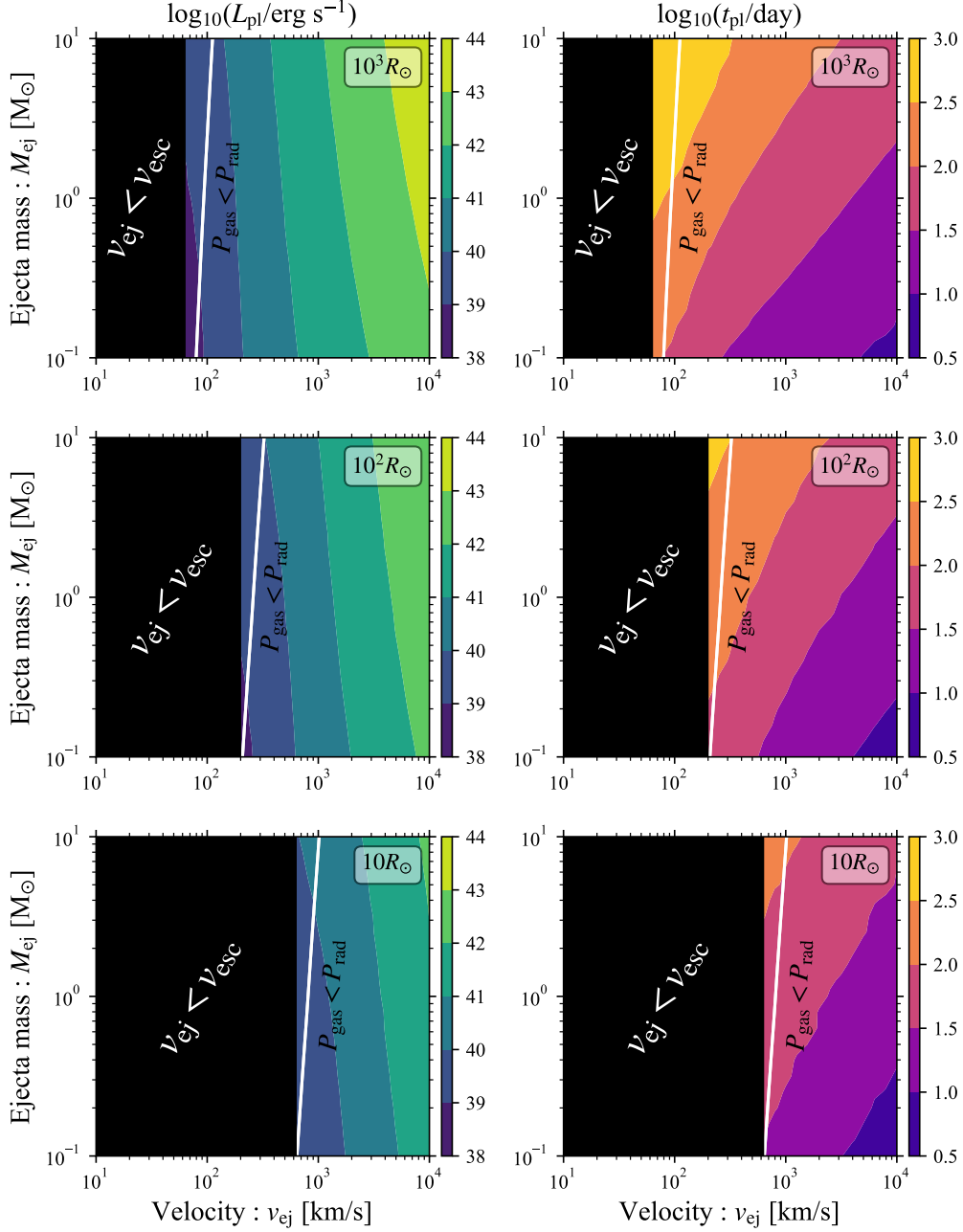


Figure 4. Contours of the characteristic optical precursor luminosity L_{pl} (after subtracting the UV luminosity; left column) and duration t_{pl} (right column) associated with eruptive mass-loss events in the space of ejecta velocity and mass, for different initial radii $R_0 = 10^3, 10^2,$ and $10 R_\odot$ (from top to bottom). Black shaded regions are excluded because the ejecta velocity is smaller than the surface escape speed for a star of mass $M_\star = 10 M_\odot$ and radius $R_\star \leq R_0$. To the right of the white contours radiation-pressure exceeds gas-pressure at the initial radius.

ferred (albeit usually on larger radial scales; e.g., [Smith 2014](#)). As described in Sec. 2.2, the total light curve is obtained by adding those from successive single shells (an example of which is shown by a thin black curve in Fig. 5). Since the total luminosity approaches a steady-state on the timescale roughly set by the characteristic duration of the single shell emission, we denote the latter t_{rise} and calculate its value in the same way as the eruption model at the stationary state (i.e., it is defined by the timescale over which 90% of energy is radiated). The rise-time is roughly equal to that over which photons diffuse out from the shell, t_d (Eq. 14).

The single-shell light curve exhibits a gradual rise followed by sharp peak, powered by the escape of energy that accompanies a rapid decrease in the photon diffusion timescale at hydrogen recombination. For the fiducial model, radiation pressure dominates (marginally) over gas pressure during the recombination phase, rendering the contribution of recombination energy to the radiated energy small. The luminosity reached during the steady plateau phase is roughly given by the product of the single shell’s characteristic luminosity calculated in the same way as in the eruption model (dividing the radiated energy by t_{rise}), by the number of shells ejected during the rise phase $\simeq t_{\text{rise}}/\Delta t$. We remark that the rise-time $t_{\text{rise}}(\sim t_d)$ is independent of the choice of shell thickness $v\Delta t$ because it does not enter in Eq. (14).

Colored curves in Fig. 5 show additional light curve calculations varying the wind mass-loss rates and velocities from the fiducial model. Because the rise-time is roughly set by the diffusion timescale $t_d \propto \dot{M}/v_w$ (Eq. 14), the steady-state luminosity is achieved faster for higher wind velocities. Similarly, winds with higher mass-loss rates take longer to reach steady-state.

As an aside, we remark that for winds with low velocities and/or high- \dot{M} , our calculation overestimates the photosphere radius and hence underestimates (by less than a factor of $\lesssim 2$) the effective temperature of the emission. As a result of the shallow wind density profile $\rho \propto r^{-2}$, material ahead of the recombination front (which quickly cools to $\lesssim 10^3$ K) can contribute significantly to the optical depth through molecular absorption. However, at such low temperatures, our analytic opacity law (which adopts a constant value $\kappa_{\text{mol}} = 0.1Z \sim 10^{-3} \text{ cm}^2 \text{ g}^{-1}$) overestimates the true molecular opacity. Unless significant dust formation occurs to boost the opacity further ([Freedman et al. 2008](#); [Pejcha et al. 2016](#)), the true photosphere location should therefore coincide with the recombination front, at somewhat smaller radii than our model predicts.

The top panels of Fig. 6 show the rise-time t_{rise} (upper right panel) and steady-state luminosity L_{pl} (upper left panel) as a function of the wind velocity v_w and mass-loss rate \dot{M} , for fixed progenitor mass $M_\star = 10 M_\odot$. Regions of the phase space for which the wind kinetic energy is below the Eddington luminosity of the star are blacked out, based on the expectation that the star

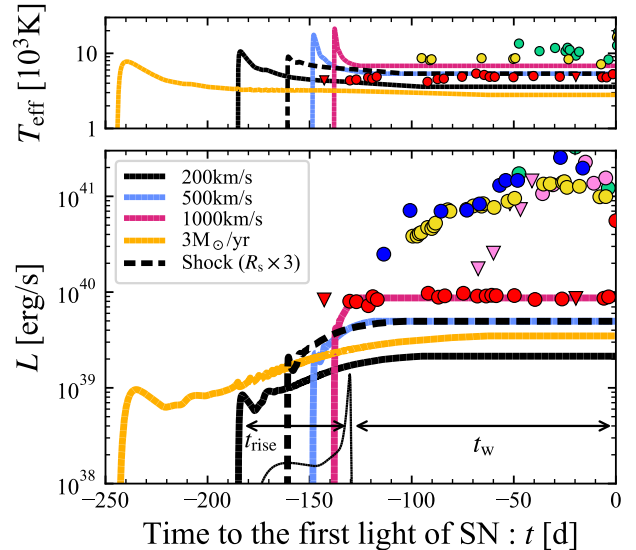


Figure 5. Optical light curves of SN precursor emission in the wind mass-loss scenario for progenitor mass $M_\star = 10 M_\odot$. A thick black curve shows the fiducial case with wind mass-loss rate $\dot{M} = 1 M_\odot \text{ yr}^{-1}$ and wind velocity $v_w = 200 \text{ km s}^{-1}$ ($R_s = 10^2 R_\odot$). The wind duration is set to $t_w = 130 \text{ d}$ to match the SN2020tlf precursor duration (shown for comparison red points, along with the other precursors labeled as in Fig. 1). A thin black curve shows the light curve from a single shell of thickness $\Delta t = 4 \text{ d}$ for the fiducial model, whose duration—being similar for all shells—controls the rise-time of the total light curve. Colored lines show the light curve that results by increasing the wind mass-loss rate or speed relative to the fiducial model (while fixing t_w). A black dashed curve shows the effect of tripling the “sonic” radius at which the wind thermal energy is initialized, to crudely mimic the effects of re-heating of the ejecta by internal shocks (Sec. 3.2.1).

would respond to sub-Eddington energy deposition by driving convection or expanding, rather than give rise to significant mass-loss (e.g., [Quataert et al. 2016](#)). Likewise, regions for which the total mass-loss in wind ejecta experienced over the light curve rise-time, exceeds the total stellar mass (i.e., $M_{\text{ej}} \simeq \dot{M} t_{\text{rise}} > M_\star$) are shaded gray. As shown in Fig. 7, this condition imposes severe limits on the wind scenario. White shaded regions denote the mass-loss rate $\dot{M}(v_w)$ predicted by [Quataert et al. \(2016\)](#) (Eq. 18) for a range of heated envelope masses $M_{\text{env}} \sim 10^{-3} - 10^{-1} M_\star$.

In Appendix A we derive analytic estimates of the steady-state luminosity as a function of the wind properties. There are two regimes to consider, depending on whether the ejecta is still ionized or has begun to recombine by the radius of emission (as dictated by whether \dot{M} is below or above, respectively, a critical value \dot{M}_{ion} ;

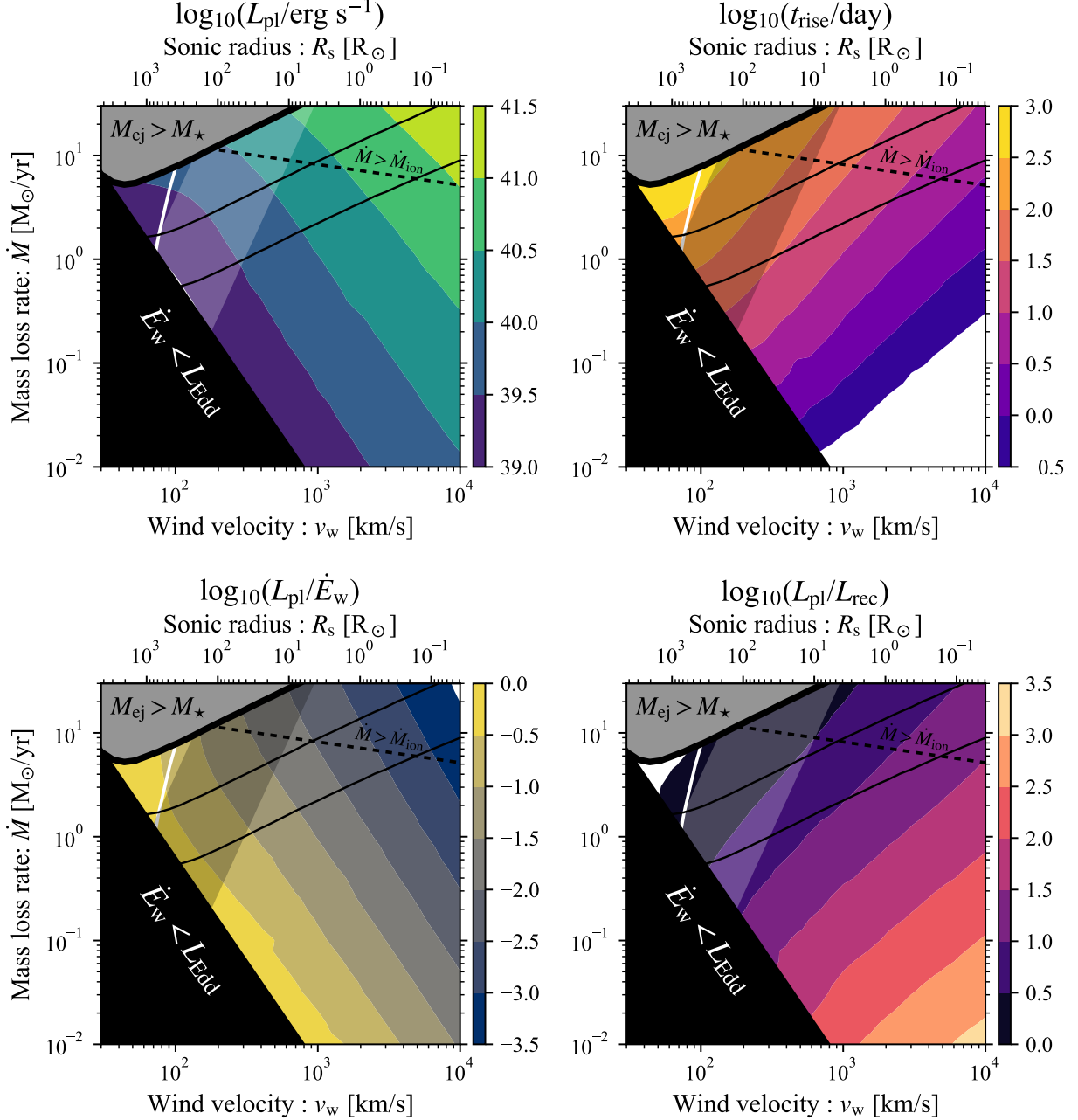


Figure 6. *Top:* Steady-state L_{pl} luminosity (left panel) and rise-time t_{rise} (right panel) of SN precursor emission from wind-like mass-ejection as a function of the wind mass-loss rate \dot{M} and velocity v_w (equivalently, sonic radius for an assumed progenitor star mass $M_{\star} = 10 M_{\odot}$; top horizontal axis). Black and gray shaded regions are excluded based on the wind kinetic luminosity being sub-Eddington and the total ejecta mass during the rise-time exceeding the progenitor star mass (Eq. A8). The other solid black lines correspond to $M_{\text{ej}} = 0.1M_{\star}$ and $0.01M_{\star}$. Thin shaded regions represent the mass-loss rate $\dot{M}(v_w)$ predicted by Quataert et al. (2016) (Eq. 18), for a range of envelope masses $M_{\text{env}}/M_{\star} = 0.001 - 0.1$. A black dashed line shows the critical mass-loss rate \dot{M}_{ion} (Eq. A7 for $T_{\text{ion}} = 10^4$ K) above which the drop in opacity from hydrogen recombination determines the transient rise-time. Radiation pressure exceeds gas pressure at the sonic point to the right of the white line, i.e. across most of the parameter space. *Bottom:* Same as top panels, but showing the ratios of steady-state L_{pl} luminosity to the wind kinetic power, \dot{E}_w (Eq. A2; left panel), and to the maximum recombination luminosity, L_{rec} (Eq. 21; right panel).

Eq. A7). For $\dot{M} < \dot{M}_{\text{ion}}$ we find $L \propto \dot{M}^{1/3} v_w^{2/3}$ (Eq. A3; see also Quataert et al. 2016; Shen et al. 2016), while for $\dot{M} > \dot{M}_{\text{ion}}$ we find $L \propto \dot{M}^{3/4} v_w^{3/4}$ (Eq. A6). These dependencies roughly agree with our findings in Figs. 5, 6.

The bottom left panel of Fig. 6 shows the ratio of steady-state transient luminosity to the wind kinetic power L_{pl}/\dot{E}_w , i.e., a measure of the wind’s radiative efficiency. The efficiency decreases as the wind power $\dot{E}_w \propto M v_w^2$ increases, roughly according to $L_{\text{pl}}/\dot{E}_w \propto (\dot{E}_w/L_{\text{Edd}})^{-2/3}$ (see Eq. A3). Larger values of \dot{M} push the diffusion radius ($\sim v_w t_d$) outwards, while larger v_w shrink the sonic radius, both effects of which result in greater adiabatic losses prior to where radiation can escape from the wind.

The bottom right panel of Fig. 6 shows the ratio of L_{pl} to maximum recombination luminosity,

$$L_{\text{rec}} = \frac{\varepsilon_{\text{H}} X \dot{M}}{m_{\text{p}}} \simeq 6.1 \times 10^{38} \text{ erg s}^{-1} \left(\frac{\dot{M}}{M_{\odot} \text{ yr}^{-1}} \right), \quad (21)$$

where $\varepsilon_{\text{H}} = 13.6 \text{ eV}$ is the recombination energy per hydrogen atom of mass m_{p} and $X = 0.74$ is the hydrogen mass fraction of the ejecta at solar metallicity. Unlike in the case of most stellar merger transients (Metzger et al. 2021; Matsumoto & Metzger 2022), the radiated luminosity generally exceeds the recombination luminosity insofar as radiation pressure dominates over gas pressure (as satisfied to the right of the solid white line in Fig. 6).

For $\dot{M} < \dot{M}_{\text{ion}}$, we invert Eqs. (14), (A3) to obtain the wind mass-loss rate and velocity in terms of the observed precursor luminosity and rise-time⁵:

$$v_w \simeq 940 \text{ km s}^{-1} \left(\frac{M_{\star}}{10 M_{\odot}} \right)^{-2/3} \left(\frac{t_{\text{rise}}}{10 \text{ d}} \right)^{-1/3} \left(\frac{L_{\text{pl}}}{10^{40} \text{ erg s}^{-1}} \right), \quad (22)$$

$$\dot{M} \simeq 1.5 M_{\odot} \text{ yr}^{-1} \left(\frac{M_{\star}}{10 M_{\odot}} \right)^{-2/3} \left(\frac{t_{\text{rise}}}{10 \text{ d}} \right)^{2/3} \left(\frac{L_{\text{pl}}}{10^{40} \text{ erg s}^{-1}} \right). \quad (23)$$

These expressions reveal that very large mass-loss rates $\dot{M} \gtrsim 1 - 10 M_{\odot} \text{ yr}^{-1}$ are required to explain the SN precursor luminosities, $L_{\text{pre}} \sim 10^{40} - 10^{41} \text{ erg s}^{-1}$. In fact, a conservative upper limit can be placed on the steady-state plateau luminosity in the wind-scenario under the condition that total wind ejecta mass M_{ej} not exceed the progenitor star mass. This translates into an upper limit on the wind mass-loss rate: $M_{\text{ej}} = t_{\text{active}} \dot{M} < M_{\star}$,

⁵ Constraining the rise-time is challenging in practice because current observations do not probe the earliest stages of the precursor emission (Fig. 1); furthermore, the luminosity evolves slowly even before reaching steady-state, making it hard to cleanly distinguish the rising phase.

where t_{active} is the duration of mass-loss episode (from the wind launch to the SN explosion). This timescale may be reasonably approximated by the longer of the (theoretical) light curve rise-time, t_{rise} , or the observed precursor plateau duration, t_{pre} . For t_{rise} , the maximal \dot{M} and corresponding maximum steady-state luminosity L_{max} are derived in Appendix A (Eqs. A9, A11). For t_{pre} , the maximal luminosity follows by substituting $\dot{M} = \dot{M}_{\text{max}} = M_{\star}/t_{\text{pre}}$ into Eqs. (A3), (A6). We set the maximal luminosity by taking the smaller one calculated for t_{rise} and t_{pre} .

This theoretical maximum luminosity is shown with a solid black line in Fig. 7 as a function of v_w for $M_{\star} = 10 M_{\odot}$ and a plateau duration $t_{\text{pre}} = 100 \text{ d}$ close to those observed (Fig. 1). For lower wind speeds $v_w \lesssim 1000 \text{ km s}^{-1}$, the light curve rise-time exceeds the observed plateau duration $t_{\text{rise}} > t_{\text{pre}}$, placing the tighter limit on the maximal luminosity. For comparison, colored symbols show the time-averaged luminosities and spectroscopically-measured outflow velocities for individual SN precursors (Table 1). The precursor luminosities typically exceed the theoretical limit by at least a factor of a few, thus challenging the wind scenario.

In precursor events for which flash-spectroscopy observations were conducted soon after the SN explosion, the measured CSM velocities from these observations (v_{obs} in Table 1) are in two cases (SN 2016bdu and SN 2020tlf) so low the SN ejecta would have swept up any precursor-ejected material before the observations were taken (hence, the CSM velocities measured must arise from an earlier mass-loss episode prior to the precursor rise). This hypothetical requirement on the measurable CSM velocity can be written:

$$v_{\text{obs}} \gtrsim v_{\text{engulf}} \equiv v_{\text{SN}} \frac{t_{\text{flash}}}{t_{\text{pre}}} \simeq 1000 \text{ km s}^{-1} \left(\frac{v_{\text{SN}}}{10^4 \text{ km s}^{-1}} \right) \left(\frac{t_{\text{flash}}}{10 \text{ d}} \right) \left(\frac{t_{\text{pre}}}{100 \text{ d}} \right)^{-1}, \quad (24)$$

where v_{SN} and t_{flash} are the SN ejecta velocity and time of the flash-spectroscopy observation measured since the SN explosion, respectively.⁶ As a corollary, CSM with velocities $v_{\text{obs}} > v_{\text{engulf}}$ could in principle (if present) be observed in systems with flash spectroscopy observations, thus enabling an upper limit on $v_w < v_{\text{engulf}}$ based on the lack of detection. This maximal observable velocity v_{engulf} are shown as left-facing arrows in Fig. 7 for $v_{\text{SN}} = 10^4 \text{ km s}^{-1}$.

⁶ Note that here we define the critical velocity not by the entire wind active period t_{active} but rather the observed duration t_{pre} ; this is justified because emission from the maximal CSM velocity material typically rises quickly $t_{\text{rise}} \lesssim t_{\text{pre}}$.

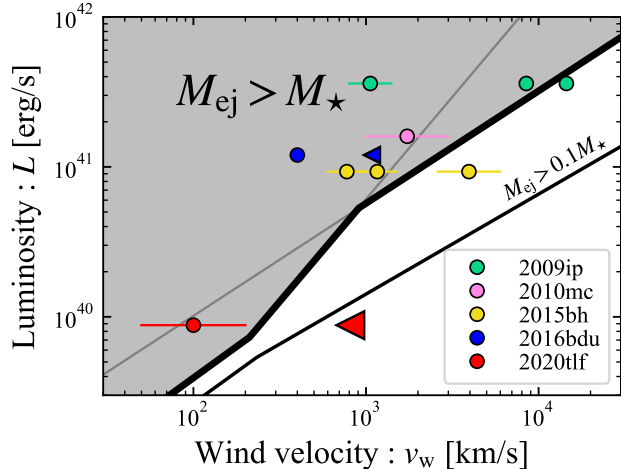


Figure 7. The steady wind scenario is challenged to explain high luminosities of SN precursor emission for reasonable ejecta masses. Black lines show the maximum steady-state luminosity in the wind scenario as a function of wind velocity so as not to overproduce the total wind ejecta mass M_{ej} (Eqs. A9, A11); specifically, the gray shaded region is excluded by the requirement $M_{\text{ej}} > M_{\star} = 10 M_{\odot}$ (see text for details). Colored circles represent observed SN precursor luminosities and velocities (Table 1). Left-directed triangles show an estimate of the wind velocity (v_{engulf} ; Eq. 24) invisible to flash spectroscopy observations (too slow wind material would be overtaken by the SN shock prior to the observations).

Taken together, we conclude that only SN 2020tlf can be explained by the wind scenario for a reasonable ejecta mass $\lesssim 0.1 M_{\star} \sim M_{\odot}$, and in this case only if the wind velocity (inaccessible to flash spectroscopy) were to obey $600 \text{ km s}^{-1} \lesssim v_w \lesssim 1000 \text{ km s}^{-1}$. These values could be consistent with a RSG progenitor whose envelope mass outside of the implied sonic radius $R_s \sim 10 R_{\odot}$ is on the order of $\sim M_{\odot}$. Interestingly, these parameters are also consistent with the wind solution of Quataert et al. (2016) for the envelope mass of $M_{\text{env}} \sim 10^{-4} - 10^{-5} M_{\star}$. Given the implied small sonic radius of $R_s \sim 10 R_{\odot}$, we can estimate the mass included between the energy injection and sonic radii by $M_{\text{env}} \sim \dot{M} R_s / v_w \sim 10^{-5} M_{\odot} \sim 10^{-4} M_{\star}$, consistent with the required value of M_{env} .

3.2.1. Shock Interaction

A potential mechanism to boost the luminosity of the wind is through shock interaction. By reheating the wind ejecta well above the sonic surface, shocks reduce the adiabatic losses experienced before the flow reaches the diffusion radius where the remaining thermal energy is radiated (Eq. A1). One source of shock interaction

are internal collisions within the wind itself, due to time variability in the wind speed.

Consider two shells with the same mass M but different velocities. The slower shell with velocity v is ejected δt before the faster one with velocity $(1 + \delta_v)v$. The latter one catches up with former one in a time $\delta t / \delta_v$ and they merge to form a single shell. The collision radius is estimated by $R_{\text{col}} \sim (2 + 1/\delta_v)R_s$, where we have assumed both shells originate from the same radius $\sim R_s$ separated by a time $\delta t \sim R_s/v$ roughly equal to the dynamical time at the launching surface. From momentum and energy conservation, the final velocity of the merged-shell is $(1 + \delta_v/2)v$ and the energy dissipated by the collision is $M(v\delta_v)^2/2$.

The velocity difference δ_v has two competing effects on the radiated luminosity of the shocked wind. While smaller values of δ_v increase the collision radius and thus reduce the adiabatic losses, such collisions also dissipate less energy than for larger δ_v . Adiabatic losses exterior to R_{col} reduce the observed luminosity by an amount $L \propto R_{\text{col}}^{-2/3} \propto (2 + 1/\delta_v)^{-2/3}$ (Eq. A2), while the boost in thermal energy $\propto (\delta_v)^2$; cases with the largest, order-unity fluctuations $\delta_v \sim 1$ therefore give the biggest luminosity boost.

To demonstrate the potential effects of shock heating, we recalculate the fiducial wind scenario light curve for the (most luminous) case $\delta_v = 1$ by artificially increasing the “sonic” radius R_s , at which the wind thermal energy is initialized in our calculation, by a factor of three compared to the fiducial case. As shown in Fig. 5, the radiated luminosity roughly doubles compared to the case without shock interaction. Our simplified treatment of the effects of shock heating results in a smooth plateau-shaped light curve similar to the case without shocks. In reality, however, the light curve should exhibit variability due to the stochastic nature of the heating, though this could be smoothed out by photon diffusion effects. Most SN precursor light curves are not perfectly smooth (Fig. 1), with the exception of SN 2020tlf (for which shock heating is anyways not strictly required in the wind scenario; Fig. 7).

Another source of shock interaction is between the wind and pre-existing CSM ejected earlier from the star,⁷ or, equivalently, if the wind velocity rises in time. In fact, Quataert et al. (2016) found that shock interaction inevitably happens before the wind settles into a steady state. After the onset of energy injection below the stellar surface, the stellar envelope is initially only weakly accelerated to form a slowly-expanding atmosphere. Continuous heating decreases the density at the heating site, accelerating the material there to higher velocity (Eq. 17). The high-speed wind then col-

⁷ Hypothetical dense clumps bound to and accumulating around the progenitor may also play a role of the dense CSM (Soker 2021).

lides with the slowly-expanding atmosphere, generating shocks which can dominate the radiated luminosity, at least initially. Although we defer a detailed study to future work, shock interaction due to an accelerating wind provide another way to increase the wind’s radiative efficiency, particularly at early times.

4. PRECURSOR-GENERATED CSM

The mass ejected from the progenitor star during the precursor phase becomes a source of CSM for shock interaction with the SN ejecta following the explosion. The application of our precursor light curve models to individual events enables us to constrain their ejecta masses and velocities, which we can then check for consistency with the CSM properties inferred by modeling interaction signatures during the SN phase.

4.1. Eruption scenario

We have found (Sec. 3.1) that the eruption scenario can account for the luminosities and timescales of SN precursor emission for physically reasonable ejecta properties. The ejecta mass and initial radius in this scenario are obtained by inverting Eqs. (19), (20) in terms of the precursor luminosity L_{pl} and duration t_{pl} :

$$M_{\text{ej}} \simeq 6.7 M_{\odot} \left(\frac{v_{\text{ej}}}{10^3 \text{ km s}^{-1}} \right)^3 \left(\frac{t_{\text{pl}}}{100 \text{ d}} \right)^4 \left(\frac{L_{\text{pl}}}{10^{41} \text{ erg s}^{-1}} \right)^{-1}, \quad (25)$$

$$R_0 \simeq 140 R_{\odot} \left(\frac{v_{\text{ej}}}{10^3 \text{ km s}^{-1}} \right)^{-4} \left(\frac{t_{\text{pl}}}{100 \text{ d}} \right)^{-2} \left(\frac{L_{\text{pl}}}{10^{41} \text{ erg s}^{-1}} \right)^2. \quad (26)$$

Unfortunately, these estimates depend sensitively on the ejecta speed v_{ej} , which is challenging to measure and comes with large uncertainties. Furthermore, the observed precursor duration t_{pre} provides only a lower limit on the total duration (t_{pl}) which enters these formulae if the SN prematurely terminates the precursor emission.

Table 2 provides the ejecta mass, kinetic energy ($E_{\text{kin}} = M_{\text{ej}} v_{\text{obs}}^2/2$), and progenitor radius for our precursor sample (Table 1) as obtained from the inverted Popov formulae (Eqs. 25, 26). Again, the observed precursor duration is only a lower limit on the total plateau duration and hence we obtain only a lower (upper) limit on the ejecta mass (progenitor radius). All values are calculated assuming lowest spectroscopically observed velocity range. However, we again caution that our estimates are highly dependent on the adopted ejecta speed; a factor of two difference in the velocity changes the results by an order of magnitude or more.

At the time of the SN explosion, the characteristic outer radius and density of the precursor ejecta (here-

Table 2. CSM Properties implied by Eruption Model

Event	$M_{\text{ej}}^{(a)}$ [M_{\odot}]	$E_{\text{kin}}^{(a)}$ [10^{48} erg]	$R_0^{(b)}$ [$10^3 R_{\odot}$]
SN 2009ip	0.036 – 0.19	0.23 – 3.8	2.4 – 23
SN 2010mc	0.039 – 1.0	0.39 – 94	0.046 – 3.7
SN 2015bh	1.3 – 5.9	4.6 – 59	0.13 – 1.0
SN 2016bdu	0.32	0.51	8.4
SN 2020tlf	0.025 – 1.6	0.00062 – 0.63	0.42 – 110

Note. All quantities calculated by applying the observed precursor properties (Table 1) to Eqs. (25), (26), assuming the lowest spectroscopically observed velocity (which gives the most physical ejecta mass; Fig. 8).

(a) Lower limit, based on the requirement that $t_{\text{pl}} > t_{\text{pre}}$.

(b) Upper limit, based on the requirement that $t_{\text{pl}} > t_{\text{pre}}$.

after CSM) are thus given, respectively, by

$$R_{\text{CSM}} \sim v_{\text{ej}} t_{\text{pre}} \simeq 8.6 \times 10^{14} \text{ cm} \left(\frac{v_{\text{ej}}}{10^3 \text{ km s}^{-1}} \right) \left(\frac{t_{\text{pre}}}{100 \text{ d}} \right), \quad (27)$$

$$\rho_{\text{CSM}} \sim \frac{M_{\text{ej}}}{\frac{4\pi}{3} R_{\text{CSM}}^3} \gtrsim 5.0 \times 10^{-12} \text{ g cm}^{-3} \times \left(\frac{t_{\text{pre}}}{100 \text{ d}} \right) \left(\frac{L_{\text{pre}}}{10^{41} \text{ erg s}^{-1}} \right)^{-1}, \quad (28)$$

where the second equality in Eq. (28) makes use of Eq. (25). The upper limit on ρ_{CSM} results because $t_{\text{pl}} > t_{\text{pre}}$ and is notably independent of the (poorly constrained) ejecta velocity.

The left panel of Fig. 8 shows the estimated CSM density ρ_{CSM} and radius R_{CSM} in the eruption scenario for the observed precursors (Fig. 1, Table 1). As discussed in Sec. 3.1 and shown in Fig. 3, the required CSM masses are typically in the range $\sim 0.1 - 1 M_{\odot}$. Since the light curve properties depend only weakly on the ejecta velocity profile $M_{\text{ej}} \propto v^{-\beta}$ (Eq. 8), the slope of the resulting CSM radial density profile $\rho \propto r^{-\beta-3}$ (at $r > R_{\text{CSM}}$ or equivalently $v > v_{\text{ej}}$) is not well-constrained by the precursor observations. However, as long as $\beta \gtrsim 0$, the CSM mass will be concentrated in the $\sim v_{\text{ej}}$ shell on the radial scale $\sim R_{\text{CSM}}$.

Several implications follow from the implied CSM properties. The inferred CSM is sufficiently massive and compact as to be optically thick ($\rho \gtrsim 10^{-14} \text{ g cm}^{-3} (R_{\text{CSM}}/10^{14} \text{ cm})^{-1}$), thus implying that (1) the SN shock breakout will occur from the precursor-generated CSM shell instead of the original stellar surface; (2) flash spectroscopy cannot readily probe the mean velocity of the precursor ejecta (though it may probe its high-velocity tail).

Shock heating of the CSM shell by the supernova ejecta will dissipate the kinetic energy of the latter and boost the luminosity of the supernova relative to the CSM-free case. The luminosity of this shock interaction can be crudely estimated as⁸

$$L_{\text{sh}} \sim \frac{\frac{1}{2}\varepsilon M_{\text{ej}} v_{\text{SN}}^2}{t_{\text{diff}}} \frac{R_{\text{CSM}}}{v_{\text{SN}} t_{\text{diff}}} \simeq 6 \times 10^{42} \text{ erg s}^{-1} \left(\frac{\varepsilon}{0.1}\right) \left(\frac{R_{\text{CSM}}}{10^{14} \text{ cm}}\right) \left(\frac{v_{\text{SN}}}{10^4 \text{ km s}^{-1}}\right)^2, \quad (29)$$

where $t_{\text{diff}} = \sqrt{\frac{\kappa M_{\text{ej}}}{4\pi c v_{\text{SN}}}}$ is the characteristic photon diffusion time through the shocked CSM, and ε is the radiative efficiency. Interestingly, the luminosity depends only on the CSM radius. For CSM radii $R_{\text{CSM}} \simeq 3 \times 10^{14} \text{ cm}$ implied by the precursor emission (Fig. 4) the predicted luminosities $L_{\text{sh}} \sim 10^{43} \text{ erg s}^{-1}$ broadly agree with those of the SNe following the precursor events (Fig. 1). However, for SN 2020tlf with $R_{\text{CSM}} \sim 10^{14} \text{ cm}$, the shock-boosted SN luminosity would be too low and another CSM component, for example optically-thick CSM extending to large radii $\sim 10^{15} \text{ cm}$, is required to power the early SN light curve via CSM interaction.

Though constraints on the CSM properties from the literature of our precursor sample are limited, we comment briefly on those available. For SN 2009ip, [Margutti et al. \(2014\)](#); [Moriya \(2015\)](#) interpret the SN emission as arising due to shock breakout emission from a dense shell produced by the precursor outburst; they estimate a precursor mass of $\sim 0.1 M_{\odot}$ and radius $\sim 10^{15} \text{ cm}$ at explosion, by equating the SN rise-time to the photon diffusion time through the dense shell. Our result is essentially consistent with theirs for this event, for an assumed ejecta velocity equal to the lowest measured spectroscopically, $v_{\text{ej}} \simeq 800 - 1400 \text{ km s}^{-1}$. For SN 2020tlf, [Chugai & Utrobin \(2022\)](#) model the precursor emission as arising from an ejecta mass of $M_{\text{ej}} \sim 0.1 M_{\odot}$, also consistent with our result. They find that subsequent SN emission is not affected by this compact CSM, but that an additional wind-like CSM extending up to $\sim 10^{15} \text{ cm}$ is required (we return to this event within the context of the wind-scenario in the next section).

4.2. Wind scenario

Detecting the rising phase of the light curve in the wind scenario is typically challenging (see Fig. 5). We therefore assume that the emission has already reached its stationary state by the time of the observations. Inverting Eq. (A3), we derive the required wind mass-loss

rate in terms of observed precursor properties:

$$\dot{M} \simeq 1.5 M_{\odot} \text{ yr}^{-1} \left(\frac{M_{\star}}{10 M_{\odot}}\right)^{-2} \times \left(\frac{v_{\text{w}}}{10^3 \text{ km s}^{-1}}\right)^{-2} \left(\frac{L_{\text{pre}}}{10^{40} \text{ erg s}^{-1}}\right)^3. \quad (30)$$

Insofar as the outer radius of the wind ejecta at the time of the SN explosion is given by $R_{\text{CSM}} \sim v_{\text{w}} t_{\text{active}} \gtrsim v_{\text{w}} t_{\text{pre}}$, Eq. (27) with v_{ej} replaced by v_{w} gives a lower limit on R_{CSM} while the rise-time is typically shorter than t_{pre} for relevant wind velocities. This in turn implies an upper limit on the CSM density at R_{CSM} ,

$$\rho_{\text{CSM}} = \frac{\dot{M}}{4\pi R_{\text{CSM}}^2 v_{\text{w}}} \lesssim 1.0 \times 10^{-13} \text{ g cm}^{-3} \left(\frac{M_{\star}}{10 M_{\odot}}\right)^{-2} \times \left(\frac{v_{\text{w}}}{10^3 \text{ km s}^{-1}}\right)^{-5} \left(\frac{L_{\text{pre}}}{10^{40} \text{ erg s}^{-1}}\right)^3 \left(\frac{t_{\text{pre}}}{100 \text{ d}}\right)^{-2}. \quad (32)$$

which depends sensitively on the wind velocity. Assuming the wind mass-loss rate is roughly constant prior to the SN, the CSM density at $r < R_{\text{CSM}}$ will follow a wind-like $\rho \propto r^{-2}$ profile.

The right panel of Fig. 8 shows the estimated CSM density of observed precursors in the wind mass-loss scenario. As discussed in Sec. 3.2, the required CSM density, or equivalently mass-loss rate \dot{M} , is enormous, exceeding that allowed by the total mass budget of the star in most events.

Only in SN 2020tlf can the observed precursor be reasonably accommodated, for the maximally-allowed velocity $v_{\text{w}} \sim v_{\text{engulf}} \simeq 10^3 \text{ km s}^{-1}$ (and we note that $\dot{M} \simeq \text{const}$ mass-loss may indeed be suggested for this event by the flat shape of the precursor light curve). The implied radial extent of the CSM $\sim 10^{15} \text{ cm}$ in the wind scenario is consistent with an upper limit based on X-ray non-detections ([Jacobson-Galán et al. 2022](#)) and light-curve modeling ([Chugai & Utrobin 2022](#)) (though we note that the density required in our scenario is 3 – 10 times greater than found by these authors). Given uncertainties on parameters, such as the progenitor mass and wind velocity, and potential for internal-shock-heating (Sec. 3.2.1), this level of discrepancy may nevertheless be tolerable. We note that the CSM radius obtained for SN 2020tlf in the eruption scenario (Table 2) is also consistent with the modeling of [Chugai & Utrobin \(2022\)](#).

As in the eruption case, the inferred CSM density (wind mass-loss rate) should not be so large that it overproduces the SN luminosity via CSM shock interaction. For freely expanding SN ejecta into a wind-like density profile, the SN luminosity can be estimated as

⁸ This scaling differs from that for interacting SN with wind-like CSM because of the steeper density profile.

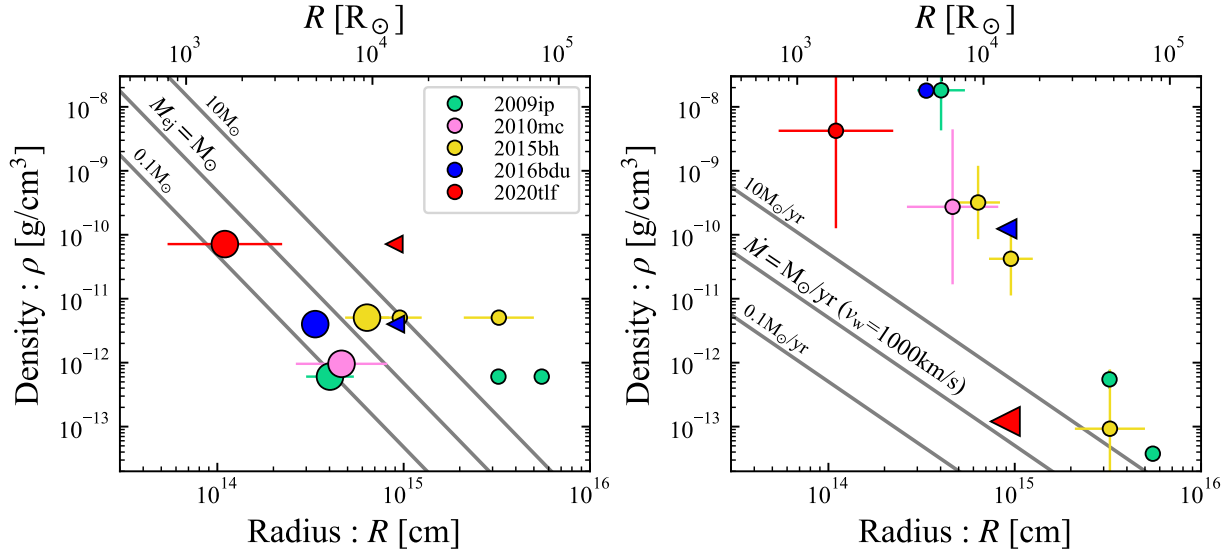


Figure 8. CSM density profile resulting from eruption (left) and wind (right) mass-loss models. The gray lines in left (right) panel show corresponding ejecta mass (mass-loss rate) of $M_{\text{ej}}(\dot{M}) = 0.1, 1,$ and $10 M_{\odot}$ ($M_{\odot} \text{ yr}^{-1}$). For the same event, different points are calculated by different velocity obtained by observations (see Table 1).

(e.g., Chevalier & Irwin 2011, but here ignoring deceleration of the shocked CSM shell):

$$L_{\text{sh}} \sim \frac{\frac{1}{2}\varepsilon M_{\text{swpt}} v_{\text{SN}}^2}{t_{\text{diff}}} \quad (33)$$

$$\simeq 3 \times 10^{43} \text{ erg s}^{-1} \left(\frac{\varepsilon}{0.1}\right) \left(\frac{\dot{M}}{M_{\odot} \text{ yr}^{-1}}\right) \times \left(\frac{v_{\text{SN}}}{10^4 \text{ km s}^{-1}}\right)^3 \left(\frac{v_w}{10^3 \text{ km s}^{-1}}\right)^{-1}, \quad (34)$$

where $M_{\text{swpt}} \sim \rho R_{\text{diff}}^3$ is the CSM wind mass swept-up by SN ejecta on the wind diffusion timescale $t_{\text{diff}} = \frac{\kappa \dot{M}}{4\pi c v_w}$ (Eq. 6), and we assumed the radius $R_{\text{diff}} \sim v_{\text{SN}} t_{\text{diff}} \sim 6 \times 10^{14} \text{ cm} (\dot{M}/M_{\odot} \text{ yr}^{-1})(v_{\text{SN}}/10^4 \text{ km s}^{-1})(v_w/10^3 \text{ km s}^{-1})^{-1}$ is smaller than the outer edge of the CSM, R_{CSM} .

The estimate for L_{sh} in the case of SN 2020tlf is roughly consistent with its SN luminosity, while we find $L_{\text{sh}} \gg L_{\text{SN}}$ given the much higher values \dot{M} required to explain other precursors. This again favors the eruption scenario over the steady-wind scenario as the origin of most SN precursors, at least neglecting shock-heating within the wind (Sec. 3.2.1).

5. SUMMARY

We have modeled the precursor optical emission detected from a growing sample of core collapse SNe using an extension of the semi-analytical light curve model described in Matsumoto & Metzger (2022). The observed precursors can be regarded as extreme cases of the mass-loss events increasingly inferred to occur just before the terminal collapse, whose direct emission can

provide clues to the nature of the mass-loss mechanisms at work and more generally about the final stages of massive star evolution. We develop light curve models in the context of two scenarios (‘eruption’ and ‘wind’) for the nature of the pre-SN mass-loss phase.

In the eruption model, energy is deposited near the base of stellar envelope on a timescale shorter than the dynamical time. While our model is indifferent to the mechanism responsible for this energy injection, it could in principle be caused by a violent outburst associated with late stages of nuclear shell burning. This sudden energy deposition creates a shock wave, which propagates outwards towards the surface of the star, ejecting a portion of its envelope. For the eruption scenario, our findings are summarized as follows:

- The eruption light curve is characterized by a recombination-driven plateau similar to that of Type IIP SNe (Fig. 3). The luminosity and duration of the plateau are reasonably estimated by the so-called “Popov formulae” (Popov 1993) which relates these observables to the ejecta mass and progenitor radius (Eqs. 19, 20). However, because the entirety of precursor light curve is generally not observable (due to interruption by the SN explosion), we can obtain only lower limits on the ejecta mass M_{ej} and kinetic energy E_{kin} for individual events. Adopting an ejecta velocity $v_{\text{obs}} \sim 100 - 1000 \text{ km s}^{-1}$ consistent with those inferred from spectroscopy, the observed precursor luminosities are reproduced for $M_{\text{ej}} \gtrsim 0.1 - 1 M_{\odot}$ and $E_{\text{kin}} \gtrsim 10^{48} - 10^{50} \text{ erg}$ (Table 2). We caution that the latter estimate depends sensitively on the

ejecta velocity, which is not available in all events and could in principle be confused with CSM from other, earlier phases of mass-loss.

- A wide range of precursor luminosities can be produced in this model, $L_{\text{pre}} \sim 10^{39} - 10^{42} \text{ erg s}^{-1}$ (Fig. 4, see also Dessart et al. 2010). The luminosity mainly depends on the progenitor radius and ejecta velocity. Bright precursors of $L_{\text{pre}} \gtrsim 10^{41} \text{ erg s}^{-1}$ require large progenitor radii $R_* \gtrsim 10^2 R_\odot$ such as RSGs. For these progenitors, super-Eddington luminosities $L_{\text{pre}} \gtrsim L_{\text{Edd}} \sim 10^{39} \text{ erg s}^{-1}$ ($M_*/10 M_\odot$) are achieved only for the ejecta speeds larger than the escape speed of the stellar surface, supporting the source of energy deposition occurring deep inside the stellar envelope.

The second scenario we considered is one of steady wind-like mass-loss, which results from a continuous energy deposition at the base of stellar envelope (mainly motivated by the wave-heating scenario; e.g., Quataert & Shiode 2012; Fuller 2017). For the wind scenario, our findings are summarized as follows:

- The light curve undergoes a gradual rise, before settling into a stationary state. The rise-time is essentially given by the diffusion timescale of the wind, and the steady-state luminosity as $L \sim L_{\text{Edd}} (\frac{1}{2} \dot{M} v_w^2 / L_{\text{Edd}})^{1/3}$ (Eq. A3, A6; see also Quataert et al. 2016; Shen et al. 2016). For typical values of the observed precursor ejecta velocity, very large mass-loss rates $\dot{M} \gtrsim 10 M_\odot \text{ yr}^{-1}$ are required to achieve the observed precursor luminosities $L_{\text{pre}} \sim 10^{41} \text{ erg s}^{-1}$ (Fig. 6). Such large mass-loss rates would also increase the light curve rise-time which (in conjunction with the large required \dot{M}) would exceed the mass budget of the star. This constraint can be formalized by defining a theoretical maximum precursor luminosity for a given wind velocity (Fig. 7; Appendix A).

Among the five well-observed precursors in our sample, only SN 2020tlf with its relatively low luminosity, can be explained by the wind model, for a mass-loss rate of $\dot{M} \simeq 1 M_\odot \text{ yr}^{-1}$ and velocity of $v_w \simeq 10^3 \text{ km s}^{-1}$. The corresponding sonic radius is again deep inside the star, $R_s \sim 10 R_\odot \ll 10^2 - 10^3 R_\odot$, requiring energy deposition at the base of stellar envelope.

- The luminosity of the wind can be boosted due to internal shocks, for instance due to a time-variable wind speed, by a modest factor $\lesssim 2$. However, the relatively smooth observed shape of the precursor light curves may disfavor shock interaction.

While we do not study them in detail, external shocks between the precursor ejecta and pre-existing CSM may also take place and contribute to the luminosity (see also Quataert et al. 2016;

Strotjohann et al. 2021; Jacobson-Galán et al. 2022). The shock luminosity can be crudely estimated by energy and momentum conservation. Neglecting any losses of efficiency due to deceleration of wind, the shock-dissipated energy is given by $E_{\text{sh}} \sim \frac{1}{2} \left(\frac{M_w M_{\text{pCSM}}}{M_w + M_{\text{pCSM}}} \right) v_w^2$, where $M_w = \dot{M} t_{\text{pre}}$ is the wind mass ejected during the precursor and M_{pCSM} is the pre-existing CSM mass swept up by the wind. For pre-existing CSM with a wind-like profile, the swept-up mass is given by $M_{\text{pCSM}} = \int^{v_w t_{\text{pre}}} 4\pi r^2 \rho_{\text{pCSM}} dr = \dot{M}_{\text{pCSM}} v_w t_{\text{pre}} / v_{\text{pCSM}}$, where \dot{M}_{pCSM} and v_{pCSM} are the mass-loss rate and velocity of the pre-existing CSM, respectively. Combining results, the radiated shock luminosity is given by

$$L_{\text{sh}} \sim \frac{E_{\text{sh}}}{t_{\text{pre}}} \sim \left(\frac{1}{1 + r_\rho} \right) \dot{E}_w, \quad (35)$$

where $r_\rho = \rho_w / \rho_{\text{pCSM}}$ is independent of r for wind-like profiles. While $r_\rho > 1$ is required to neglect deceleration of the wind, and hence $L_{\text{sh}} \lesssim \dot{E}_w$, the stronger dependence of the radiated luminosity on \dot{E}_w in Eq. (35) than Eq. (A3) suggests that shock interaction can still dominate over the intrinsic wind luminosity. Future work is needed to explore the external shock scenario in greater detail.

- Absent external shock interaction, the fact that observed SN precursors violated the maximal luminosity in the wind scenario may favor eruptive events (e.g., driven by unstable nuclear shell burning) over a more continuous heating source (e.g., due to wave heating).

In both eruption and wind models, the precursor ejecta forms an optically-thick compact CSM shell surrounding the progenitor star that will be present at the time of collapse and could boost the luminosity of the supernova light curve substantially through shock interaction. Our main finding is:

- The radial extent of the CSM is typically so small $R_{\text{CSM}} \lesssim 10^{15} \text{ cm}$ (see Eq. 27) that it is engulfed by SN ejecta less than ten days after SN explosion. Therefore, flash spectroscopy carried out a few days after SN may miss the signature of the precursor ejecta and probe only the CSM released before the precursor mass-loss episode (see also Strotjohann et al. 2021). In the eruption model, the density profile of the CSM is steeper than the steady wind profile ($\rho \propto r^{-2}$), forming a dense CSM core.

ACKNOWLEDGMENTS

We thank Avishay Gal-Yam and Eliot Quataert for helpful comments on an early draft of the text. This work is supported in part by JSPS Overseas Research Fellowships (T.M.). B.D.M. acknowledges support from the National Science Foundation (grant number AST-2009255).

APPENDIX

A. ANALYTIC ESTIMATES OF PRECURSOR EMISSION IN THE WIND MASS-LOSS SCENARIO

The rise-time of the precursor light curve (equivalently, the duration of the single shell light curve; Fig. 5) is determined by the diffusion timescale through the shell, t_d (Eq. 14). Radiation thus escapes the wind ejecta from the characteristic radius

$$R_d \simeq v_w t_d = \frac{\kappa \dot{M}}{4\pi c} \simeq 5.4 \times 10^{13} \text{ cm} \left(\frac{\dot{M}}{M_\odot \text{ yr}^{-1}} \right). \quad (\text{A1})$$

In this appendix, we normalize κ to the fully-ionized electron scattering opacity, $\kappa_{\text{es}} \simeq 0.32 \text{ cm}^2 \text{ g}^{-1}$. Because photons are trapped, the wind material expands adiabatically between the sonic and diffusion radii ($R_s < r < R_d$), such that $T \propto \rho^{1/3} \propto r^{-2/3}$ under radiation-pressure-dominated condition and $\rho \propto r^{-2}$ for a steady wind. The thermal and kinetic luminosities of the wind are comparable at R_s ; thus, the photon (advection) luminosity $L \simeq 4\pi r^2 v_w a T^4 \propto T^4 r^2 \propto r^{-2/3}$ evolves as

$$L \simeq \dot{E}_w \left(\frac{r}{R_s} \right)^{-2/3}, \quad (\text{A2})$$

up to the diffusion becomes important. Here \dot{E}_w is the wind kinetic power (Eq. 12).

There are two cases to consider, depending on whether the wind material remains fully ionized or has begun to recombine below $\sim R_d$. When \dot{M} is sufficiently low (the precise threshold, \dot{M}_{ion} , to be defined below), the ejecta is still fully ionized ($T \gtrsim T_{\text{ion}} \simeq 10^4 \text{ K}$) when photons start to diffuse out of the wind. Inserting Eq. (A1) into Eq. (A2), we find

$$L = L_{\text{Edd}} \left(\frac{\dot{E}_w}{L_{\text{Edd}}} \right)^{1/3} \simeq 3.2 \times 10^{39} \text{ erg s}^{-1} M_{\star,1}^{2/3} \left(\frac{\dot{M}}{M_\odot \text{ yr}^{-1}} \right)^{1/3} \left(\frac{v_w}{200 \text{ km s}^{-1}} \right)^{2/3}, \quad \dot{M} < \dot{M}_{\text{ion}}, \quad (\text{A3})$$

where $M_{\star,1} = M_\star / (10 M_\odot)$. This expression agrees with previous works (e.g., Quataert et al. 2016; Shen et al. 2016).

On the other hand, when \dot{M} is sufficiently large, hydrogen recombination begins below R_d , which triggers photon diffusion by reducing the opacity $\kappa \ll \kappa_{\text{es}}$ and effectively shrinking the diffusion radius. Recombination occurs at the temperature $T = T_{\text{ion}} = 10^4 T_{\text{ion},4} \text{ K}$, as is achieved at the radius

$$R_{\text{ion}} = R_s \left(\frac{T_s}{T_{\text{ion}}} \right)^{3/2} = \left(\frac{\dot{M}^3 (2GM_\star)^2}{(8\pi a T_{\text{ion}}^4)^3 v_w} \right)^{1/8} \simeq 2.5 \times 10^{14} \text{ cm} M_{\star,1}^{1/4} T_{\text{ion},4}^{-3/2} \left(\frac{\dot{M}}{M_\odot \text{ yr}^{-1}} \right)^{3/8} \left(\frac{v_w}{200 \text{ km s}^{-1}} \right)^{-1/8}, \quad (\text{A4})$$

on the timescale

$$t_{\text{ion}} = \frac{R_{\text{ion}}}{v_w} \simeq 140 \text{ d} M_{\star,1}^{1/4} T_{\text{ion},4}^{-3/2} \left(\frac{\dot{M}}{M_\odot \text{ yr}^{-1}} \right)^{3/8} \left(\frac{v_w}{200 \text{ km s}^{-1}} \right)^{-9/8}, \quad (\text{A5})$$

where

$$T_s = \left(\frac{\dot{M} v_w}{8\pi a R_s^2} \right)^{1/4} = \left(\frac{\dot{M} v_w^5}{8\pi a (2GM_\star)^2} \right)^{1/4} \simeq 1.1 \times 10^5 \text{ K} M_{\star,1}^{-1/2} \left(\frac{\dot{M}}{M_\odot \text{ yr}^{-1}} \right)^{1/4} \left(\frac{v_w}{200 \text{ km s}^{-1}} \right)^{5/4}$$

is the wind temperature at the sonic radius. The wind luminosity in the high- \dot{M} case (Eq. A2) is then given by

$$L = \dot{E}_w \left(\frac{R_{\text{ion}}}{R_s} \right)^{-2/3} = L_{\text{Edd}} \left(\frac{\dot{E}_w}{L_{\text{Edd}}} \right)^{1/3} \left(\frac{\dot{M}}{\dot{M}_{\text{ion}}} \right)^{5/12} = \left(\frac{\pi a T_{\text{ion}}^4 (2GM_\star)^2 \dot{M}^3 v_w^3}{2} \right)^{1/4},$$

$$\simeq 1.2 \times 10^{39} \text{ erg } M_{\star,1}^{1/2} T_{\text{ion},4} \left(\frac{\dot{M}}{M_\odot \text{ yr}^{-1}} \right)^{3/4} \left(\frac{v_w}{200 \text{ km s}^{-1}} \right)^{3/4}, \quad \dot{M} > \dot{M}_{\text{ion}}. \quad (\text{A6})$$

The critical mass-loss rate above which recombination defines the transient luminosity can be estimated by equating Eqs. (A3) and (A6),

$$\dot{M}_{\text{ion}} = \left(\frac{2^7 \pi^5 (2GM_\star)^2 c^8}{a^3 \kappa^8 T_{\text{ion}}^{12} v_w} \right)^{1/5} \simeq 11 M_\odot \text{ yr}^{-1} M_{\star,1}^{2/5} T_{\text{ion},4}^{-12/5} \left(\frac{v_w}{200 \text{ km s}^{-1}} \right)^{-1/5}. \quad (\text{A7})$$

For precursor emission which exhibits a steady-state plateau-like light curve, the mass-loss must be active for a timescale $\gtrsim t_d$ (t_{ion}). For a given allowed ejecta mass M_{ej} , this implies a maximum on the wind mass-loss rate can be obtained. For the low- \dot{M} case, demanding $t_d \dot{M} < M_{\text{ej}}$ gives

$$\dot{M}_{\text{max}} = \left(\frac{4\pi c v_w M_{\text{ej}}}{\kappa} \right)^{1/2} \simeq 11 M_\odot \text{ yr}^{-1} M_{\star,1}^{1/2} \left(\frac{M_{\text{ej}}}{M_\star} \right)^{1/2} \left(\frac{v_w}{200 \text{ km s}^{-1}} \right)^{1/2}, \quad (\text{A8})$$

and corresponding maximal steady-state luminosity is given by

$$L_{\text{max}} = 7.0 \times 10^{39} \text{ erg s}^{-1} M_{\star,1}^{5/6} \left(\frac{M_{\text{ej}}}{M_\star} \right)^{1/6} \left(\frac{v_w}{200 \text{ km s}^{-1}} \right)^{5/6}. \quad (\text{A9})$$

On the other hand, for the low \dot{M} case, the maximal mass-loss rate and luminosity are given by

$$\dot{M}_{\text{max}} = \left(\frac{(8\pi a T_{\text{ion}}^4)^3 v_w^9 M_{\text{ej}}^8}{(2GM_\star)^2} \right)^{1/11} \simeq 11 M_\odot \text{ yr}^{-1} M_{\star,1}^{6/11} T_{\text{ion},4}^{12/11} \left(\frac{M_{\text{ej}}}{M_\star} \right)^{8/11} \left(\frac{v_w}{200 \text{ km s}^{-1}} \right)^{9/11}, \quad (\text{A10})$$

$$L_{\text{max}} = 6.8 \times 10^{39} \text{ erg s}^{-1} M_{\star,1}^{10/11} T_{\text{ion},4}^{20/11} \left(\frac{M_{\text{ej}}}{M_\star} \right)^{6/11} \left(\frac{v_w}{200 \text{ km s}^{-1}} \right)^{15/11}. \quad (\text{A11})$$

REFERENCES

- Aguilera-Dena, D. R., Langer, N., Moriya, T. J., & Schootemeijer, A. 2018, *ApJ*, 858, 115, doi: [10.3847/1538-4357/aabfc1](https://doi.org/10.3847/1538-4357/aabfc1)
- Arnett, W. D. 1980, *ApJ*, 237, 541, doi: [10.1086/157898](https://doi.org/10.1086/157898)
- . 1982, *ApJ*, 253, 785, doi: [10.1086/159681](https://doi.org/10.1086/159681)
- Bilinski, C., Smith, N., Li, W., et al. 2015, *MNRAS*, 450, 246, doi: [10.1093/mnras/stv566](https://doi.org/10.1093/mnras/stv566)
- Blagorodnova, N., Klencki, J., Pejcha, O., et al. 2021, *A&A*, 653, A134, doi: [10.1051/0004-6361/202140525](https://doi.org/10.1051/0004-6361/202140525)
- Boian, I., & Groh, J. H. 2018, *A&A*, 617, A115, doi: [10.1051/0004-6361/201731794](https://doi.org/10.1051/0004-6361/201731794)
- Bruch, R. J., Gal-Yam, A., Schulze, S., et al. 2021, *ApJ*, 912, 46, doi: [10.3847/1538-4357/abef05](https://doi.org/10.3847/1538-4357/abef05)
- Chakraborti, S., Ray, A., Smith, R., et al. 2016, *ApJ*, 817, 22, doi: [10.3847/0004-637X/817/1/22](https://doi.org/10.3847/0004-637X/817/1/22)
- Chandra, P., Chevalier, R. A., Chugai, N., et al. 2012, *ApJ*, 755, 110, doi: [10.1088/0004-637X/755/2/110](https://doi.org/10.1088/0004-637X/755/2/110)
- Chatzopoulos, E., Wheeler, J. C., Vinko, J., Horvath, Z. L., & Nagy, A. 2013, *ApJ*, 773, 76, doi: [10.1088/0004-637X/773/1/76](https://doi.org/10.1088/0004-637X/773/1/76)
- Chevalier, R. A. 2012, *ApJL*, 752, L2, doi: [10.1088/2041-8205/752/1/L2](https://doi.org/10.1088/2041-8205/752/1/L2)
- Chevalier, R. A., & Irwin, C. M. 2011, *ApJL*, 729, L6, doi: [10.1088/2041-8205/729/1/L6](https://doi.org/10.1088/2041-8205/729/1/L6)
- Chiba, Y., Katsuda, S., Yoshida, T., Takahashi, K., & Umeda, H. 2020, *PASJ*, 72, 25, doi: [10.1093/pasj/psz148](https://doi.org/10.1093/pasj/psz148)
- Chugai, N., & Utrobin, V. 2022, arXiv e-prints, arXiv:2205.07749. <https://arxiv.org/abs/2205.07749>
- Dessart, L., Livne, E., & Waldman, R. 2010, *MNRAS*, 405, 2113, doi: [10.1111/j.1365-2966.2010.16626.x](https://doi.org/10.1111/j.1365-2966.2010.16626.x)
- Dwarkadas, V. V., Romero-Cañizales, C., Reddy, R., & Bauer, F. E. 2016, *MNRAS*, 462, 1101, doi: [10.1093/mnras/stw1717](https://doi.org/10.1093/mnras/stw1717)

- Elias-Rosa, N., Pastorello, A., Benetti, S., et al. 2016, MNRAS, 463, 3894, doi: [10.1093/mnras/stw2253](https://doi.org/10.1093/mnras/stw2253)
- Elias-Rosa, N., Van Dyk, S. D., Benetti, S., et al. 2018, ApJ, 860, 68, doi: [10.3847/1538-4357/aac510](https://doi.org/10.3847/1538-4357/aac510)
- Fields, C. E., & Couch, S. M. 2021, ApJ, 921, 28, doi: [10.3847/1538-4357/ac24fb](https://doi.org/10.3847/1538-4357/ac24fb)
- Filippenko, A. V. 1997, ARA&A, 35, 309, doi: [10.1146/annurev.astro.35.1.309](https://doi.org/10.1146/annurev.astro.35.1.309)
- Foley, R. J., Berger, E., Fox, O., et al. 2011, ApJ, 732, 32, doi: [10.1088/0004-637X/732/1/32](https://doi.org/10.1088/0004-637X/732/1/32)
- Foley, R. J., Smith, N., Ganeshalingam, M., et al. 2007, ApJL, 657, L105, doi: [10.1086/513145](https://doi.org/10.1086/513145)
- Fox, O. D., Chevalier, R. A., Skrutskie, M. F., et al. 2011, ApJ, 741, 7, doi: [10.1088/0004-637X/741/1/7](https://doi.org/10.1088/0004-637X/741/1/7)
- Fransson, C., Sollerman, J., Strotjohann, N. L., et al. 2022, arXiv e-prints, arXiv:2206.06497. <https://arxiv.org/abs/2206.06497>
- Fraser, M., Stritzinger, M. D., Brennan, et al. 2021, arXiv e-prints, arXiv:2108.07278. <https://arxiv.org/abs/2108.07278>
- Fraser, M., Inserra, C., Jerkstrand, A., et al. 2013, MNRAS, 433, 1312, doi: [10.1093/mnras/stt813](https://doi.org/10.1093/mnras/stt813)
- Freedman, R. S., Marley, M. S., & Lodders, K. 2008, ApJS, 174, 504, doi: [10.1086/521793](https://doi.org/10.1086/521793)
- Fuller, J. 2017, MNRAS, 470, 1642, doi: [10.1093/mnras/stx1314](https://doi.org/10.1093/mnras/stx1314)
- Fuller, J., & Ro, S. 2018, MNRAS, 476, 1853, doi: [10.1093/mnras/sty369](https://doi.org/10.1093/mnras/sty369)
- Gal-Yam, A., & Leonard, D. C. 2009, Nature, 458, 865, doi: [10.1038/nature07934](https://doi.org/10.1038/nature07934)
- Gal-Yam, A., Leonard, D. C., Fox, D. B., et al. 2007, ApJ, 656, 372, doi: [10.1086/510523](https://doi.org/10.1086/510523)
- Gal-Yam, A., Arcavi, I., Ofek, E. O., et al. 2014, Nature, 509, 471, doi: [10.1038/nature13304](https://doi.org/10.1038/nature13304)
- Gal-Yam, A., Bruch, R., Schulze, S., et al. 2022, Nature, 601, 201, doi: [10.1038/s41586-021-04155-1](https://doi.org/10.1038/s41586-021-04155-1)
- Gandel'Man, G. M., & Frank-Kamenetskii, D. A. 1956, Soviet Physics Doklady, 1, 223
- Ginzburg, S., & Balberg, S. 2012, ApJ, 757, 178, doi: [10.1088/0004-637X/757/2/178](https://doi.org/10.1088/0004-637X/757/2/178)
- Graham, M. L., Sand, D. J., Valenti, S., et al. 2014, ApJ, 787, 163, doi: [10.1088/0004-637X/787/2/163](https://doi.org/10.1088/0004-637X/787/2/163)
- Graham, M. L., Bigley, A., Mauerhan, J. C., et al. 2017, MNRAS, 469, 1559, doi: [10.1093/mnras/stx948](https://doi.org/10.1093/mnras/stx948)
- Humphreys, R. M., & Davidson, K. 1994, PASP, 106, 1025, doi: [10.1086/133478](https://doi.org/10.1086/133478)
- Jacobson-Galán, W. V., Dessart, L., Jones, D. O., et al. 2022, ApJ, 924, 15, doi: [10.3847/1538-4357/ac3f3a](https://doi.org/10.3847/1538-4357/ac3f3a)
- Jencson, J. E., Sand, D. J., Andrews, J. E., et al. 2022, arXiv e-prints, arXiv:2206.02816. <https://arxiv.org/abs/2206.02816>
- Jiang, Y.-F., Cantiello, M., Bildsten, L., et al. 2018, Nature, 561, 498, doi: [10.1038/s41586-018-0525-0](https://doi.org/10.1038/s41586-018-0525-0)
- Johnson, S. A., Kochanek, C. S., & Adams, S. M. 2018, MNRAS, 480, 1696, doi: [10.1093/mnras/sty1966](https://doi.org/10.1093/mnras/sty1966)
- Kasen, D., & Ramirez-Ruiz, E. 2010, ApJ, 714, 155, doi: [10.1088/0004-637X/714/1/155](https://doi.org/10.1088/0004-637X/714/1/155)
- Kasen, D., & Woosley, S. E. 2009, ApJ, 703, 2205, doi: [10.1088/0004-637X/703/2/2205](https://doi.org/10.1088/0004-637X/703/2/2205)
- Khazov, D., Yaron, O., Gal-Yam, A., et al. 2016, ApJ, 818, 3, doi: [10.3847/0004-637X/818/1/3](https://doi.org/10.3847/0004-637X/818/1/3)
- Kiewe, M., Gal-Yam, A., Arcavi, I., et al. 2012, ApJ, 744, 10, doi: [10.1088/0004-637X/744/1/10](https://doi.org/10.1088/0004-637X/744/1/10)
- Ko, T., Tsuna, D., Takei, Y., & Shigeyama, T. 2021, arXiv e-prints, arXiv:2112.14909. <https://arxiv.org/abs/2112.14909>
- Kochanek, C. S., Beacom, J. F., Kistler, M. D., et al. 2008, ApJ, 684, 1336, doi: [10.1086/590053](https://doi.org/10.1086/590053)
- Kochanek, C. S., Fraser, M., Adams, S. M., et al. 2017, MNRAS, 467, 3347, doi: [10.1093/mnras/stx291](https://doi.org/10.1093/mnras/stx291)
- Kuriyama, N., & Shigeyama, T. 2020, A&A, 635, A127, doi: [10.1051/0004-6361/201937226](https://doi.org/10.1051/0004-6361/201937226)
- Leung, S.-C., & Fuller, J. 2020, ApJ, 900, 99, doi: [10.3847/1538-4357/abac5d](https://doi.org/10.3847/1538-4357/abac5d)
- Levesque, E. M., Stringfellow, G. S., Ginsburg, A. G., Bally, J., & Keeney, B. A. 2014, AJ, 147, 23, doi: [10.1088/0004-6256/147/1/23](https://doi.org/10.1088/0004-6256/147/1/23)
- Linial, I., Fuller, J., & Sari, R. 2021, MNRAS, 501, 4266, doi: [10.1093/mnras/staa3969](https://doi.org/10.1093/mnras/staa3969)
- Margutti, R., Milisavljevic, D., Soderberg, A. M., et al. 2014, ApJ, 780, 21, doi: [10.1088/0004-637X/780/1/21](https://doi.org/10.1088/0004-637X/780/1/21)
- Margutti, R., Kamble, A., Milisavljevic, D., et al. 2017, ApJ, 835, 140, doi: [10.3847/1538-4357/835/2/140](https://doi.org/10.3847/1538-4357/835/2/140)
- Martin, J. C., Hamsch, F. J., Margutti, R., et al. 2015, AJ, 149, 9, doi: [10.1088/0004-6256/149/1/9](https://doi.org/10.1088/0004-6256/149/1/9)
- Matsumoto, T., & Metzger, B. D. 2022, arXiv e-prints, arXiv:2202.10478. <https://arxiv.org/abs/2202.10478>
- Mauerhan, J., Williams, G. G., Smith, N., et al. 2014, MNRAS, 442, 1166, doi: [10.1093/mnras/stu730](https://doi.org/10.1093/mnras/stu730)
- Mauerhan, J. C., Smith, N., Filippenko, A. V., et al. 2013, MNRAS, 430, 1801, doi: [10.1093/mnras/stt009](https://doi.org/10.1093/mnras/stt009)
- McDowell, A. T., Duffell, P. C., & Kasen, D. 2018, ApJ, 856, 29, doi: [10.3847/1538-4357/aaa96e](https://doi.org/10.3847/1538-4357/aaa96e)
- Mcley, L., & Soker, N. 2014, MNRAS, 445, 2492, doi: [10.1093/mnras/stu1952](https://doi.org/10.1093/mnras/stu1952)
- Meakin, C. A., & Arnett, D. 2007, ApJ, 667, 448, doi: [10.1086/520318](https://doi.org/10.1086/520318)

- Metzger, B. D., Zenati, Y., Chomiuk, L., Shen, K. J., & Strader, J. 2021, arXiv e-prints, arXiv:2108.04305.
<https://arxiv.org/abs/2108.04305>
- Moriya, T. J. 2015, ApJL, 803, L26,
 doi: [10.1088/2041-8205/803/2/L26](https://doi.org/10.1088/2041-8205/803/2/L26)
- Moriya, T. J., Maeda, K., Taddia, F., et al. 2014, MNRAS, 439, 2917, doi: [10.1093/mnras/stu163](https://doi.org/10.1093/mnras/stu163)
- Nakar, E., & Sari, R. 2010, ApJ, 725, 904,
 doi: [10.1088/0004-637X/725/1/904](https://doi.org/10.1088/0004-637X/725/1/904)
- Nyholm, A., Sollerman, J., Tartaglia, L., et al. 2020, A&A, 637, A73, doi: [10.1051/0004-6361/201936097](https://doi.org/10.1051/0004-6361/201936097)
- Ofek, E. O., Sullivan, M., Cenko, S. B., et al. 2013, Nature, 494, 65, doi: [10.1038/nature11877](https://doi.org/10.1038/nature11877)
- Ofek, E. O., Sullivan, M., Shaviv, N. J., et al. 2014, ApJ, 789, 104, doi: [10.1088/0004-637X/789/2/104](https://doi.org/10.1088/0004-637X/789/2/104)
- Ofek, E. O., Cenko, S. B., Shaviv, N. J., et al. 2016, ApJ, 824, 6, doi: [10.3847/0004-637X/824/1/6](https://doi.org/10.3847/0004-637X/824/1/6)
- Owocki, S. P. 2015, in Astrophysics and Space Science Library, Vol. 412, Very Massive Stars in the Local Universe, ed. J. S. Vink, 113,
 doi: [10.1007/978-3-319-09596-7_5](https://doi.org/10.1007/978-3-319-09596-7_5)
- Pastorello, A., Cappellaro, E., Inger, et al. 2013, ApJ, 767, 1, doi: [10.1088/0004-637X/767/1/1](https://doi.org/10.1088/0004-637X/767/1/1)
- Pastorello, A., & Fraser, M. 2019, Nature Astronomy, 3, 676, doi: [10.1038/s41550-019-0809-9](https://doi.org/10.1038/s41550-019-0809-9)
- Pastorello, A., Kochanek, C. S., Fraser, M., et al. 2018, MNRAS, 474, 197, doi: [10.1093/mnras/stx2668](https://doi.org/10.1093/mnras/stx2668)
- Pastorello, A., Mattila, S., Zampieri, L., et al. 2008, MNRAS, 389, 113, doi: [10.1111/j.1365-2966.2008.13602.x](https://doi.org/10.1111/j.1365-2966.2008.13602.x)
- Pastorello, A., Reguitti, A., Morales-Garoffolo, et al. 2019, A&A, 628, A93, doi: [10.1051/0004-6361/201935420](https://doi.org/10.1051/0004-6361/201935420)
- Pastorello, A., Botticella, M. T., Trundle, C., et al. 2010, MNRAS, 408, 181, doi: [10.1111/j.1365-2966.2010.17142.x](https://doi.org/10.1111/j.1365-2966.2010.17142.x)
- Pejcha, O., Metzger, B. D., & Tomida, K. 2016, MNRAS, 455, 4351, doi: [10.1093/mnras/stv2592](https://doi.org/10.1093/mnras/stv2592)
- Perley, D. A., Fremling, C., Sollerman, J., et al. 2020, ApJ, 904, 35, doi: [10.3847/1538-4357/abbd98](https://doi.org/10.3847/1538-4357/abbd98)
- Piro, A. L., & Nakar, E. 2013, ApJ, 769, 67,
 doi: [10.1088/0004-637X/769/1/67](https://doi.org/10.1088/0004-637X/769/1/67)
- Popov, D. V. 1993, ApJ, 414, 712, doi: [10.1086/173117](https://doi.org/10.1086/173117)
- Prieto, J. L., Brimacombe, J., Drake, A. J., & Howerton, S. 2013, ApJL, 763, L27, doi: [10.1088/2041-8205/763/2/L27](https://doi.org/10.1088/2041-8205/763/2/L27)
- Quataert, E., Fernández, R., Kasen, D., Klion, H., & Paxton, B. 2016, MNRAS, 458, 1214,
 doi: [10.1093/mnras/stw365](https://doi.org/10.1093/mnras/stw365)
- Quataert, E., & Shiode, J. 2012, MNRAS, 423, L92,
 doi: [10.1111/j.1745-3933.2012.01264.x](https://doi.org/10.1111/j.1745-3933.2012.01264.x)
- Reguitti, A., Pastorello, A., Pignata, G., et al. 2019, MNRAS, 482, 2750, doi: [10.1093/mnras/sty2870](https://doi.org/10.1093/mnras/sty2870)
- . 2022, arXiv e-prints, arXiv:2206.00625.
<https://arxiv.org/abs/2206.00625>
- Reilly, E., Maund, J. R., Baade, D., et al. 2017, MNRAS, 470, 1491, doi: [10.1093/mnras/stx1228](https://doi.org/10.1093/mnras/stx1228)
- Sakurai, A. 1960, Commun. Pure Appl. Math, 13, 353
- Schlegel, E. M. 1990, MNRAS, 244, 269
- Shen, R.-F., Nakar, E., & Piran, T. 2016, MNRAS, 459, 171, doi: [10.1093/mnras/stw645](https://doi.org/10.1093/mnras/stw645)
- Shiode, J. H., & Quataert, E. 2014, ApJ, 780, 96,
 doi: [10.1088/0004-637X/780/1/96](https://doi.org/10.1088/0004-637X/780/1/96)
- Smith, N. 2014, ARA&A, 52, 487,
 doi: [10.1146/annurev-astro-081913-040025](https://doi.org/10.1146/annurev-astro-081913-040025)
- Smith, N., Andrews, J. E., Filippenko, A. V., et al. 2022, arXiv e-prints, arXiv:2205.02896.
<https://arxiv.org/abs/2205.02896>
- Smith, N., & Arnett, W. D. 2014, ApJ, 785, 82,
 doi: [10.1088/0004-637X/785/2/82](https://doi.org/10.1088/0004-637X/785/2/82)
- Smith, N., Mauerhan, J. C., & Prieto, J. L. 2014, MNRAS, 438, 1191, doi: [10.1093/mnras/stt2269](https://doi.org/10.1093/mnras/stt2269)
- Smith, N., & McCray, R. 2007, ApJL, 671, L17,
 doi: [10.1086/524681](https://doi.org/10.1086/524681)
- Smith, N., & Owocki, S. P. 2006, ApJL, 645, L45,
 doi: [10.1086/506523](https://doi.org/10.1086/506523)
- Smith, N., Miller, A., Li, W., et al. 2010, AJ, 139, 1451,
 doi: [10.1088/0004-6256/139/4/1451](https://doi.org/10.1088/0004-6256/139/4/1451)
- Soker, N. 2021, ApJ, 906, 1, doi: [10.3847/1538-4357/abca8f](https://doi.org/10.3847/1538-4357/abca8f)
- Soker, N., & Kashi, A. 2013, ApJL, 764, L6,
 doi: [10.1088/2041-8205/764/1/L6](https://doi.org/10.1088/2041-8205/764/1/L6)
- Strotjohann, N. L., Ofek, E. O., Gal-Yam, A., et al. 2021, ApJ, 907, 99, doi: [10.3847/1538-4357/abd032](https://doi.org/10.3847/1538-4357/abd032)
- Sukhbold, T., Ertl, T., Woosley, S. E., Brown, J. M., & Janka, H. T. 2016, ApJ, 821, 38,
 doi: [10.3847/0004-637X/821/1/38](https://doi.org/10.3847/0004-637X/821/1/38)
- Sun, N.-C., Maund, J. R., Hirai, R., Crowther, P. A., & Podsiadlowski, P. 2020, MNRAS, 491, 6000,
 doi: [10.1093/mnras/stz3431](https://doi.org/10.1093/mnras/stz3431)
- Suzuki, A., Moriya, T. J., & Takiwaki, T. 2019, ApJ, 887, 249, doi: [10.3847/1538-4357/ab5a83](https://doi.org/10.3847/1538-4357/ab5a83)
- Svirski, G., Nakar, E., & Sari, R. 2012, ApJ, 759, 108,
 doi: [10.1088/0004-637X/759/2/108](https://doi.org/10.1088/0004-637X/759/2/108)
- Tartaglia, L., Pastorello, A., Sullivan, M., et al. 2016, MNRAS, 459, 1039, doi: [10.1093/mnras/stw675](https://doi.org/10.1093/mnras/stw675)
- Thöne, C. C., de Ugarte Postigo, A., Leloudas, G., et al. 2017, A&A, 599, A129,
 doi: [10.1051/0004-6361/201629968](https://doi.org/10.1051/0004-6361/201629968)
- Varma, V., & Müller, B. 2021, MNRAS, 504, 636,
 doi: [10.1093/mnras/stab883](https://doi.org/10.1093/mnras/stab883)
- Vink, J. S., de Koter, A., & Lamers, H. J. G. L. M. 2001, A&A, 369, 574, doi: [10.1051/0004-6361:20010127](https://doi.org/10.1051/0004-6361:20010127)

Woosley, S. E., Heger, A., & Weaver, T. A. 2002, Reviews
of Modern Physics, 74, 1015,
doi: [10.1103/RevModPhys.74.1015](https://doi.org/10.1103/RevModPhys.74.1015)

Wu, S., & Fuller, J. 2022, arXiv e-prints, arXiv:2205.03319.
<https://arxiv.org/abs/2205.03319>
Yaron, O., Perley, D. A., Gal-Yam, A., et al. 2017, Nature
Physics, 13, 510, doi: [10.1038/nphys4025](https://doi.org/10.1038/nphys4025)
Yoshida, T., Takiwaki, T., Kotake, K., et al. 2021, ApJ,
908, 44, doi: [10.3847/1538-4357/abd3a3](https://doi.org/10.3847/1538-4357/abd3a3)